CHEMICAL REVIEWS

REVIEW

pubs.acs.org/CR

Connecting the Chemical and Physical Viewpoints of What Determines Structure: From 1-D Chains to γ-Brasses

Robert F. Berger,[†,‡] Peter L. Walters,[†,§] Stephen Lee,[*,†] and Roald Hoffmann[*,†]

[†]Department of Chemistry and Chemical Biology, Cornell University, Ithaca, New York 14853, United States

[‡]Molecular Foundry, Lawrence Berkeley National Laboratory, Berkeley, California 94720, United States

[§]Department of Chemistry, University of Illinois, Urbana, Illinois 61801, United States

CONTENTS

1. INTRODUCTION

For a variety of intermetallic compounds, the per-atom valence electron count is seen as the primary determinant of the ground-state crystal structure. The remarkable relationship between structure and electron count in these so-called "electron phases", a regularity independent of the elements involved, has been illuminated by a variety of insights. The key empirical observations were made by Hume-Rothery (whose name is often attached to electron phases) over several decades in the mid-1900s.[1,2] Hume-Rothery noted that in many cases, a crystal structure exists at the same electron count for various combinations of elements. Two prototypical examples of this, both discussed in detail later in this work, are the β-brass (bcc) and γ-brass (Cu_5Zn_8[3]) structures. In phase diagrams such as those of Cu−Zn, Cu−Ga, and Cu−Sn,[4] despite the changing number of valence electrons in the element paired with Cu, the β and γ structures exist in relatively narrow composition ranges surrounding 3/2 and 21/13 valence electrons per atom, respectively.

Hume-Rothery's observations have since been supplemented by a rich literature of experimental and theoretical work. On the experimental side, some extraordinarily complex crystalline phases have been synthesized with hundreds or even thousands of atoms in their unit cells, whose stability seems to require specific ranges of valence electrons per atom. These include the Samson phases,[5−9] Vernier phases,[10−17] a variety of other compounds related to γ-brass,[18−37] and even long-period superlattices of undetermined structure whose cell axes can reach 200 nm.[38−40]

A theoretical rationale for the relationships between structural stability and valence electron count was first developed by Jones,[41] and later Mott and Jones[42] (referred to from now on collectively as MJ). Their model argues that it is favorable for a compound to adopt a structure for which the Fermi surface cuts the boundaries of the first Brillouin zone or higher zones. This perturbation-theory-based approach sees stabilization in allowing free-electron plane-wave states near the Fermi energy to mix, pushing the energies of filled states down and those of unfilled states up. Concentrating mainly on γ-brass and employing a variety of approaches, subsequent work has critically assessed the MJ model and has repeatedly affirmed its basic principles. In recent times, much of that work has involved band structure calculations, so as to properly include d orbitals.[43−50] These computations have also confirmed that the mixing of filled and unfilled states leads to a pseudogap in the density of states that is responsible for the γ-brass stability range. Other work has noted a different piece of evidence in support of Mott and Jones's arguments, namely, the rapid variation of the dielectric function near the Fermi energy.[51−53] The same concepts used to examine γ-brass have also been applied to other families of metallic structures.[54−60]

A feature shared by the MJ model and the related dielectric function-based rationale for Hume-Rothery's electron-counting

Received: April 23, 2010

   dx.doi.org/10.1021/cr1001222 | *Chem. Rev.* XXXX, XXX, 000–000

rules is that the arguments are made in reciprocal space. Chemists, whose experience is rooted in real-space structure, at times have trouble with reciprocal-space arguments. A complementary line of theoretical research has focused on real-space patterns in atomic positions. The patterns discerned have been discussed on a number of length scales, from coordination polyhedra and their organization,[21,22,61] to clusters of approximately 20−30 atoms,[3,34,62] to larger so-called "nanoclusters" and their assembly into "microframeworks",[63−65] and even to the realm of projections of higher-dimensional clusters and crystals.[66,67] Some real-space studies of γ-brass relatives have begun to delve into questions of electronic structure, but they have been more concerned with elemental site preferences than with preferred valence electron counts.[8,17,68,69]

Of course, real-space arguments have a long history of rationalizing and predicting "magic" electron counts (i.e., substantial gaps between filled and unfilled levels), and their ability to do so has contributed to chemists' inclination to stay in real space. For molecules, some of our most successful qualitative explanations for electron-counting rules use real-space, rather than momentum-space, arguments. The octet rule for main-group elements,[70,71] the 18-electron rule for transition-metal complexes,[72] Hückel's rules for π-electrons in aromatics,[73−75] and the Wade−Mingos rules for electron-deficient clusters[76,77] all rest on real-space molecular orbital models that use an atomic orbital basis set. Even in crystals there have been calculations showing that such methods can correctly reproduce the energy orderings that lead to various electron-counting rules.[78−81]

Since the MJ arguments rationalize the stability of electron phases, it should be possible to cast them in terms of real-space electronic states. Given the near-coincidence of band structures generated using models based on linear combinations of atomic orbitals (LCAO) (even those produced by the simplest extended Hückel method) and those derived from plane waves, there must exist a mapping that yields the relationship between the plane-wave electronic states relevant to the MJ model and certain LCAO. Such a real-space model could place the driving force for the stability range in electron phases as a gap between LCAO bands.

It is our goal in this work to develop such a bridging model. Sato et al.[82] have already begun to explore this linkage between nearly free electrons and LCAO, using densities of states to show for an Al−Li−Cu quasicrystal approximant how orbital hybridization splits bonding from antibonding states across the Fermi energy. The linkage has also been explored by Feng.[83] Coming from a chemical perspective, yet fully cognizant of the power of the physical argument, we will show that Hume-Rothery's observations and the MJ approach to them can be understood in the same basic way that we understand all electron-counting rules. Just as the octet and 18-electron rules stem from the energy gap between one s/p or s/p/d electronic shell and the next, the rules in Hume-Rothery electron phases arise from the mixing and splitting of an s-based band and a p-based band.

In this work, we must mix some concepts and arguments that are typically used by physicists with others that are part of the theoretical language of chemists. Therefore, in the next section, we introduce the basic concepts underlying both approaches using the simplest imaginable crystal and prepare the reader (whether nominally a physicist or a chemist) for what is to come. Later on, we review the MJ model, cast it in the language of LCAO, and discuss its validity and implications with respect to increasingly complex Hume−Rothery electron phases. We also see how the understanding gained may explain existing complex intermetallics, and predict new ones.

2. RECONCILING THE NEARLY FREE ELECTRON AND LCAO MODELS

The hypothetical crystal on which this section focuses is the one-dimensional (1-D) chain of atoms of a main-group element. We simplify the system even further by looking only at its electronic states of σ-symmetry. If asked to sketch the band structure of this crystal, physicists and chemists would likely approach the problem from very different directions—physicists in terms of the mixing of free-electron plane-wave states in the presence of a periodic potential and chemists in terms of symmetry-adapted linear combinations of atomic orbitals whose energies are shaped by bonding and antibonding interactions. While to a degree this is a caricature, that dichotomy represents our experience based on creative collaborations with both communities. There is no doubt that, as a referee notes, physicists are familiar with the LCAO model, in its tight-binding reincarnation. Even for a case as simple as this one, it takes a fair bit of thought to recognize the deep similarities between the results of these two approaches. We find it instructive to look briefly at each and then compare and contrast the two.

First, we should make a brief note about our use of mathematical notation in this paper. As often as possible, our notation is intuitive and of minimal complexity and is consistent with itself and with past work. A few conventions are worth mentioning. When employing a nearly free electron model, we refer to free-electron plane waves by lowercase ψ, nearly free electron wave functions (sums of plane waves) by capital Ψ, and the energies of either by ε. When using an LCAO model, we refer to atomic orbitals by lowercase ϕ, crystal orbitals (sums of atomic orbitals) by capital Φ, and the energies of either by ε. We refer to energy by capital E in all figures. Other issues of notation are noted in the text as they arise.

2.1. Starting with Free Electrons: The Physical Viewpoint

The static energy levels of an electron are governed by the time-independent Schrödinger equation:

$$\left[-\frac{\hbar^2}{2m}\left(\frac{\partial^2}{\partial x^2}+\frac{\partial^2}{\partial y^2}+\frac{\partial^2}{\partial z^2}\right)+V(\vec{r})\right]\Psi(\vec{r}) = \varepsilon\Psi(\vec{r})$$

For a free electron, one whose environment has no external potential, the equation is simpler:

$$-\frac{\hbar^2}{2m}\left(\frac{\partial^2}{\partial x^2}+\frac{\partial^2}{\partial y^2}+\frac{\partial^2}{\partial z^2}\right)\psi(\vec{r}) = \varepsilon\psi(\vec{r})$$

When treating a free electron, one traditionally enforces a periodic boundary condition such as the following, which assumes the eigenfunctions (electronic wave functions) repeat themselves outside of a cube of edge length $L = V^{1/3}$, a macroscopic quantity:

$$\psi(x,y,z) = \psi(x+L,y,z) = \psi(x,y+L,z) = \psi(x,y,z+L)$$

[84] The set of periodic eigenfunctions of this equation are plane waves, each of which is associated with a wavevector $\vec{k}$ whose magnitude is inversely proportional to its wavelength:

$$\psi_{\vec{k}}(\vec{r}) = \frac{1}{\sqrt{V}}e^{i\vec{k}\cdot\vec{r}}$$

dx.doi.org/10.1021/cr1001222 |Chem. Rev. XXXX, XXX, 000–000

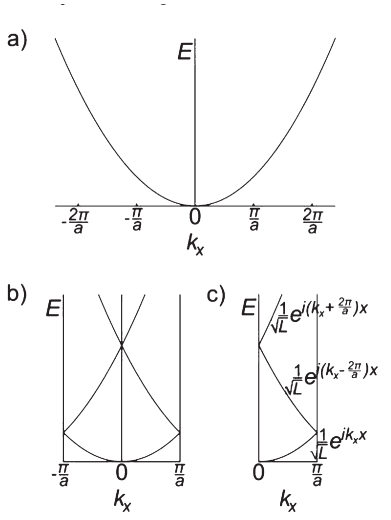

Figure 1. (a) The energy of a free-electron plane wave with respect to k_x. (b) The band structure of the empty-lattice limit of a 1-D chain of atoms, carried into the first Brillouin zone. (c) Another view of the empty-lattice limit, confined to an irreducible piece of the first Brillouin zone, with the wave function of each branch labeled.

The corresponding eigenvalues (energies) are proportional to $|\vec{k}|^2$:

$$\varepsilon_{\vec{k}} = \frac{\hbar^2}{2m}|\vec{k}|^2$$

The electrons of interest to this subsection are further constrained, for pedagogical reasons. They are free to move not throughout a 3-D space, but along one dimension, which we define as the x-axis. The Schrödinger equation and its periodic boundary condition therefore become

$$-\frac{\hbar^2}{2m}\frac{\partial^2}{\partial x^2}\psi(x) = \varepsilon\psi(x)$$

$$\psi(x) = \psi(x+L)$$

The wave functions and energies in this case are

$$\psi_{k_x}(x) = \frac{1}{\sqrt{L}}e^{ik_x x}$$

$$\varepsilon_{k_x} = \frac{\hbar^2}{2m}{k_x}^2$$

The energies of these plane-wave wave functions are proportional to ${k_x}^2$, resulting in a parabola when energy is plotted with respect to k_x (Figure 1a).

In real crystal structures, electrons are of course not free. They are subject to a periodic potential $V(\vec{r})$ created by the ions. Still, the free-electron model often proves a useful starting point for understanding crystalline electronic structure. Provided the periodic potential is relatively weak on some scale, one can think of the valence electrons in many real crystals as "nearly free". That is, the actual electronic wave functions and energies resemble those of free electrons. For a 1-D crystal, we now begin with the empty-lattice limit (where the potential tends toward zero and the electrons tend toward free electrons) and "turn on" the potential.

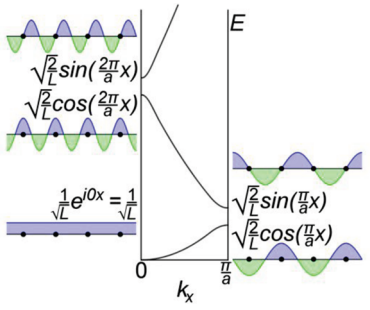

Figure 2. The nearly free electron band structure of a 1-D chain of atoms. While the wave functions and energies resemble their empty-lattice analogs far from $k_x = 0$ and $k_x = \pi/a$, the wave functions and energies near $k_x = 0$ and $k_x = \pi/a$ reflect a mixing of plane-wave states and a consequent energy splitting. Ions are shown as black circles.

Imagine that a periodic potential—for instance, that of symmetrically spaced ion cores with repeat distance a along the x-axis—is imposed on an otherwise free electron. The result is a crystal of unit cell length a, whose band structure can be concisely plotted within the first Brillouin zone ($-\pi/a \le k_x \le \pi/a$). Electronic states lying outside the first Brillouin zone can be carried into it by subtracting a reciprocal lattice vector from k_x—in this case, an integral multiple of $2\pi/a$. In the empty-lattice limit, the resulting picture (Figure1b) approaches that of a free-electron parabola appearing to fold over onto itself indefinitely. An even more concise view of this band structure (Figure 1c) uses an even smaller piece of reciprocal space, the irreducible region of the first Brillouin zone ($0 \le k_x \le \pi/a$). In the last panel of this figure, each branch of the band structure is shown along with the corresponding free-electron wave function.

The question we must now examine is how turning on the potential of a 1-D chain of ions (i.e., nuclei plus core electrons) perturbs the free-electron band structure shown in Figure 1c. As the answer is derived in detail in most introductory solid-state physics textbooks,[85,86] we only outline it here.

When an electron is subject to the periodic potential of an ion at every lattice point on the x-axis (i.e., every integral multiple of a), solutions to the Schrödinger equation are no longer pure plane waves. By Bloch's theorem, they can be written as functions of the form $\Psi_{k_x}(x) = e^{ik_x x}u_{k_x}(x)$, where $u_{k_x}(x)$ has the same periodicity as the potential $V(x)$ and can therefore be expressed as a Fourier series of plane waves. Depending on the function used to model the ionic potential, the exact form of the wave functions and electronic energies can vary. However, the qualitative picture (Figure 2) is always the same. In large part, this nearly free electron band structure remains similar to the empty-lattice limit (Figure 1c). Far from the points $k_x = 0$ and $k_x = \pi/a$ (within the range of, say, $0.2\pi/a \le k_x \le 0.8\pi/a$), the bands resemble a parabola folding over onto itself. Likewise, each wave function within this range is dominated by the corresponding free-electron plane wave. That is, states in the bottom band resemble $\Psi_{k_x}(x) = (1/L^{1/2})e^{ik_x x}$, states in the second band resemble $\Psi_{k_x}(x) = (1/L^{1/2})e^{i[k_x-(2\pi/a)]x}$, and states in the third band resemble $\Psi_{k_x}(x) = (1/L^{1/2})e^{i[k_x+(2\pi/a)]x}$.

Near the points $k_x = 0$ and $k_x = \pi/a$, however, the nearly free electron band structure looks quite different from the empty-lattice limit. Where the empty-lattice limit has pairs of plane-wave eigenstates whose energies approach degeneracy, the nearly free electron case has eigenstates that are mixtures of those plane waves whose energies are split. Take the two lowest-energy

dx.doi.org/10.1021/cr1001222 |*Chem. Rev.* XXXX, XXX, 000–000

eigenstates at $k_x = \pi/a$, for example. When a periodic potential of ion-centered wells is turned on, the eigenstates resemble a sum and a difference of two plane waves, $\Psi_{\pi/a}(x) = [1/(2L)^{1/2}]$-$(e^{i(\pi/a)x} + e^{-i(\pi/a)x}) = (2/L)^{1/2} \cos[(\pi/a)x]$ and $\Psi_{\pi/a}(x) = -[i/(2L)^{1/2}](e^{i(\pi/a)x} - e^{-i(\pi/a)x}) = (2/L)^{1/2} \sin[(\pi/a)x]$. While the size of the energy splitting between these standing-wave states depends on the strength of the ionic potential, the fundamental reason for the splitting can be seen in the visual representations of the two states on the right side of Figure 2. An electron whose wave function is $(2/L)^{1/2} \cos[(\pi/a)x]$ resides mostly near the ions, while an electron whose wave function is $(2/L)^{1/2} \sin[(\pi/a)x]$ resides mostly between the ions. If the ions were not there, the two levels would obviously be degenerate. Provided the ions are taken to be positively charged, they have a stabilizing interaction with negatively charged valence electrons, and the former eigenstate (the one concentrating electron density near the ions) is lower in energy than the latter.[87]

A similar splitting occurs at $k_x = 0$. While the lowest-energy state remains relatively unaffected by a weak external potential, the two states above it mix. The free-electron plane waves $\psi_0(x) = (1/L^{1/2})e^{i(2\pi/a)x}$ and $\psi_0(x) = (1/L^{1/2})e^{-i(2\pi/a)x}$ mix to become a sum and a difference, the standing waves $\Psi_0(x) = [1/(2L)^{1/2}](e^{i(2\pi/a)x} + e^{-i(2\pi/a)x}) = (2/L)^{1/2} \cos[(2\pi/a)x]$ and $\Psi_0(x) = -[i/(2L)^{1/2}](e^{i(2\pi/a)x} - e^{-i(2\pi/a)x}) = (2/L)^{1/2} \sin[(2\pi/a)x]$. The former wave function is lower in energy than the latter, again because its magnitude is larger near the ions.

This familiar nearly free electron band structure (Figure 2) is a qualitative picture of the electronic σ-states in a 1-D chain of atoms, derived from the starting point of plane waves. We now derive the analogous picture from the starting point of localized atomic orbitals and compare the two.

2.2. Starting with Atoms: The Chemical Viewpoint

In contrast to this physical viewpoint, which can approximate electronic states as perturbations of free-electron plane waves, the more chemical approach views them as linear combinations of atomic orbitals. One of the simplest and most transparent techniques utilizing this approach is the extended Hückel (eH) method.[88] The eH method was the first widely applied semi-empirical orbital procedure for molecules and was later applied to extended structures.

The basis set in eH consists only of atomic valence orbitals (e.g., 1s for H, 2s/2p for C, 4s/4p/3d for Fe), expressed in the form $\phi(\vec{r}) = NR(r)\, Y(\theta,\varphi)$. Radial components of the basis s and p orbitals are chosen as nodeless Slater functions, $R(r) = r^{n-1}e^{-\zeta r}$, with exponents ζ chosen by Slater's rules or to match optimized atomic functions. So-called double-ζ functions, $R(r) = r^{n-1}(c_1 e^{-\zeta_1 r} + c_2 e^{-\zeta_2 r})$, are used for d orbitals. Angular components $Y(\theta,\varphi)$ are chosen as the real form of spherical harmonics. Constants N ensure that the functions satisfy the normalization condition, $\int_{\text{all space}} \phi(\vec{r})\, \phi^*(\vec{r})\, dV = 1$.

In a *molecular* calculation, the full molecular wave functions are taken to be LCAO constructed form the atomic basis orbital:

$$\Phi_j(\vec{r}) = \sum_i C_{ij}\phi_i(\vec{r})$$

The columns of coefficients C_{ij} are eigenvectors of the following secular equation:

$$\mathbf{HC} = \varepsilon \mathbf{SC}$$

In this equation, $\boldsymbol{H}$ is an effective one-electron Hamiltonian, and $\boldsymbol{S}$ is the overlap matrix. Matrix elements $S_{ij} = \int_{\text{all space}} \phi_i(\vec{r})\, \phi_j^*(\vec{r})\, dV$ are the computed overlap integrals of the Slater-type basis functions. In contrast to the normal Hückel method, no overlap integrals are set to zero. The diagonal matrix elements H_{ii} are typically taken as valence-state ionization potentials. The off-diagonal elements H_{ij} are approximated by a Wolfsberg–Helmholtz formula:

$$H_{ij} = K\left(\frac{H_{ii} + H_{jj}}{2}\right)S_{ij}$$

with a single parameter $K = 1.75$ for all interactions. The molecular wave functions are normalized, and the corresponding eigenvalues are the one-electron eH energies. In typical eH calculations, there is no self-consistency.

Given its simplicity (only a few parameters differentiate the various basis orbitals of distinct chemical elements), the eH method (from now on we will refer to this approach descriptively as LCAO) does remarkably well in getting the correct ordering of energy levels in molecules and even the approximate energetics of angular deformations. To put it another way, LCAO gets the nodes in the right places in molecular orbitals. Extensive applications have shown the utility of the method for extended systems as well. The methodology is unreliable for total energies, but is transparent and uniquely well-adapted to generating one-electron perturbation theory-based explanations. It comes also with a suite of analytical tools—overlap populations, fragment orbital analysis, etc.—that is, to this day, unmatched in utility.

The application to extended systems is straightforward. Basis orbitals are taken not as isolated Slater-type orbitals but as Bloch functions of Slater-type orbitals. For a 1-D chain along the x-axis, with atomic spacing a and each atom labeled with an integral index n, these basis functions are (un-normalized) of the form $\Sigma_n e^{ik_x na}\phi_n(\vec{r})$. At a given k_x, there is a basis Bloch function for each valence atomic orbital in the unit cell. Therefore, when the secular equation is solved (with overlap calculations usually terminated at some long distance), the number of eigenfunctions is also equal to the number of valence atomic orbitals in the unit cell.

The qualitative features of the LCAO band structure of the 1-D chain are largely independent of which element comprises the chain. Here, the atoms are chosen to be carbon, with the following atomic parameters: H_{ii}(C 2s) = −21.4 eV, ζ_s = 1.625; H_{ii}(C 2p) = −11.4 eV, ζ_p = 1.625.[88] As in the previous subsection, our focus is only on σ-states. Thus, only 2s and $2p_x$ orbitals are used as a basis.

The band structures of two different 1-D carbon chains are shown in Figure 3. While C–C bond lengths in diamond are 1.54 Å, nearest neighbors in these chains are placed at distances of 2.2 Å (Figure 3a) and 1.9 Å (Figure 3b). The large spacings are chosen to simulate relatively weak atomic orbital interactions. Each band structure has two bands reflecting the two basis orbitals (2s and $2p_x$) on each atom, with the bottom band sloping upward and the top band sloping downward.[89] The bands in the 1.9 Å chain spread over a larger range of energies, because the shorter interatomic spacing leads to stronger bonding and antibonding interactions.

Also shown in Figure 3 are cartoons of the crystal orbitals themselves, which display s orbitals as isolated circles and p orbitals as pairs of ovals. For ease of representation, we show the crystal orbitals only at $k_x = 0$ and $k_x = \pi/a$. At other values of k_x, the atomic orbitals have complex coefficients and are therefore more difficult to represent. At $k_x = 0$, in both chains, the

dx.doi.org/10.1021/cr1001222 |Chem. Rev. XXXX, XXX, 000–000

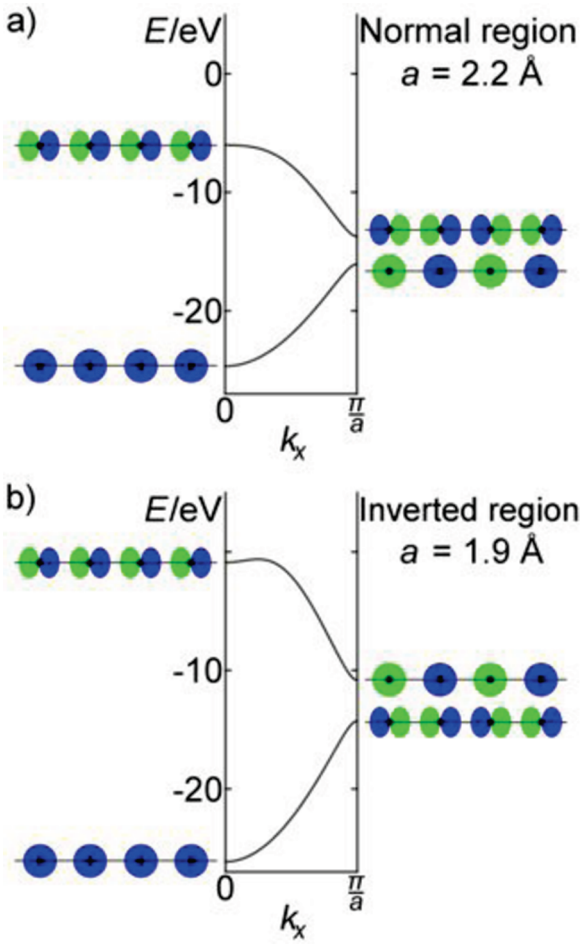

Figure 3. The LCAO band structure of a 1-D chain of carbon atoms separated by (a) 2.2 Å and (b) 1.9 Å. With the change in interatomic spacing, the energy ordering of the antibonding combination of 2s orbitals and the bonding combination of 2p orbitals at $k_x = \pi/a$ can lie in either the normal or inverted region (see the text).

lower-energy orbital is the bonding combination of 2s orbitals and the higher-energy orbital is the antibonding combination of $2p_x$ orbitals. At $k_x = \pi/a$, there is a significant difference between the electronic states of the two chains. In the 2.2 Å chain (Figure 3a), the antibonding combination of 2s orbitals is lower in energy than the bonding combination of $2p_x$ orbitals. We refer to this ordering (s antibonding below p σ-bonding) as the *normal region*, as it is what we are used to seeing in diatomic molecular orbital diagrams. In the 1.9 Å chain (Figure 3b), we see the opposite ordering. We call this the *inverted region*. In other words, when the interatomic spacing is short enough, the strength of the bonding and antibonding interactions can overcome the inherent difference in energy of 2s and 2p orbitals. Both of these regions are seen in certain experimental crystal structures.[91] We discuss the importance of the distinction, along with similarities and differences between the LCAO band structures and their nearly free electron counterpart, in the next subsection.

2.3. Different Viewpoints, Synergistic Conclusions

We have now examined the band structure of a 1-D chain of atoms using two very different approaches. It is reassuring to note that the band structures depicted in Figures 2 and 3 bear striking similarities. In both cases, the lowest-energy band slopes upward and the second band slopes downward. Even the wave functions themselves look similar. The LCAO orbitals at $k_x = 0$, the most bonding combination of 2s and the most antibonding combination of $2p_x$, closely approximate the corresponding functions $\Psi_0(x) = 1/L^{1/2}$ and $\Psi_0(x) = (2/L)^{1/2} \sin[(2\pi/a)x]$ in the nearly free electron picture. Similarly at $k_x = \pi/a$, the antibonding combination of 2s and the bonding combination of $2p_x$ resemble the nearly free electron wave functions $\Psi_{\pi/a}(x) = (2/L)^{1/2} \cos[(\pi/a)x]$ and $\Psi_{\pi/a}(x) = (2/L)^{1/2} \sin[(\pi/a)x]$.

There are some differences between the band structures in Figures 2 and 3 as well. While the nearly free electron model predicts an infinite number of bands of electronic states rising to infinitely high energies, the LCAO band structure is limited to the same number of bands as there are atomic valence orbitals in the unit cell. If the valence set were extended (say, to include 3s, 3p, and 3d), one would see more bands. The second difference, the one mentioned earlier, is in the ordering of states at $k_x = \pi/a$. While the nearly free electron model produces a band structure in the normal region (provided the ions are taken to be positively charged), the LCAO model can produce a band structure in either the normal or inverted region, depending on the element and the interatomic spacing (which dictate overlap and thus band dispersion).

Despite the differences, the feature of these band structures that is most significant to the remainder of this paper is identical in both cases. In both the nearly free electron and LCAO pictures (and in both the normal and inverted regions), there is an energy gap between the lowest-energy band and the second band, with no states lying between the two. Furthermore, in both cases, this gap is caused by the splitting of two states at $k_x = \pi/a$ that resemble standing waves whose wavelength is twice the interatomic spacing.

On the basis of this gap, one might predict that it would be energetically favorable for such a (hypothetical) 1-D chain to have two valence electrons per atom in states of σ-symmetry. If this were the case, all the lower-energy states below the gap would be filled, while all the higher-energy states above the gap would be empty. Indeed, this is the situation of maximum σ-bonding in a chain of main-group atoms. This is not to say that, when all orbitals are included (this simplified model omits π-orbitals) and pairing (Peierls) distortions allowed, the system will remain a simply bonded infinite chain.

Be that as it may, the underlying assumption that an energy gap is a favorable separator of filled states from empty states is implicit in all electron-counting rules in molecules, from the octet and 18-electron rules to Hückel's rules and Wade's rules. The assumption is also implicit in Mott and Jones's (MJ) electronic justification of the Hume-Rothery rules in solids, which is the focus of the next section.

3. THE MOTT AND JONES MODEL

The MJ model,[41,42] which was first developed in the 1930s, provides a theoretical rationale for the valence electron counts in a number of Hume-Rothery electron phases. For those unfamiliar with the model, we introduce it by example, again using the σ-states of a 1-D chain of main-group atoms. As the model is generally presented from a nearly free electron viewpoint, in terms of the mixing of plane-wave electronic states, we too begin by presenting it this way.

The arrangement of ions in a 1-D chain along the x-axis has two consequences that are important to MJ reasoning. One has already been discussed and is reiterated in Figure 4a, which

dx.doi.org/10.1021/cr1001222 |*Chem. Rev.* XXXX, XXX, 000–000

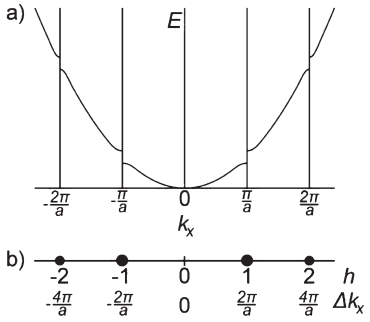

Figure 4. (a) The nearly free electron band structure of a 1-D chain of atoms, shown in the extended zone scheme. (b) The X-ray diffraction pattern of the same chain, emphasizing the correspondence between energy splittings and diffraction peaks.

employs the extended zone scheme so the bands resemble a free-electron parabola. The periodic potential causes free-electron plane-wave states of the form $\psi_{k_x}(x) = (1/L^{1/2})e^{ik_x x}$ to mix. This in turn creates energy gaps within the free-electron parabola by separating states whose electron density resides near the ions from states whose electron density resides between the ions. The lowest-energy splitting corresponds to the strong mixing of the $k_x \approx \pi/a$ states with the $k_x \approx -\pi/a$ states.[92]

Working under the assumption that a compound will adopt a structure for which the Fermi level resides in such an energy gap, this nearly free electron reasoning allows one to predict how many σ-electrons are likely to be in such a chain (if it exists as a real crystal). In this case, the states $-\pi/a \le k_x \le \pi/a$ are likely to be filled, and the others empty. As this is one unit cell of the reciprocal lattice, it translates to one filled valence σ-orbital or two valence σ-electrons, per unit cell. With just a single atom in the unit cell, the predicted valence σ-electron count for this 1-D chain is two electrons per atom.

The second important consequence of the periodic arrangement of atoms relates not to the energies of electrons but to their ability to scatter X-rays and thus create diffraction peaks. For a 3-D crystal, the relative intensities of X-ray peaks obey the proportionality

$$I_{\Delta\vec{k}} \propto \left| \sum_j f_j(\Delta\vec{k}) e^{i\Delta\vec{k}\cdot\vec{r}_j} \right|^2$$

In this summation over every atom in the crystal, $f_j(\Delta\vec{k})$ are the atomic form factors of each atom, and $\vec{r}_j$ are the spatial coordinates of each atom. In order for constructive interference to occur, $\Delta\vec{k}$ must be a reciprocal lattice vector, traditionally expressed in the form $h\vec{a}^* + k\vec{b}^* + l\vec{c}^*$ (a sum of integer multiples of the reciprocal lattice basis vectors). In our 1-D crystal, because the scattering factor of each atom is identical and all atoms lie on the x-axis, the proportionality can be simplified as follows:

$$I_{\Delta\vec{k}} \propto \left| f(\Delta\vec{k}) \sum_j e^{ih(2\pi/a)x_j} \right|^2$$

Knowing that the atoms in this chain are found at every integral multiple of a, one can verify that there are strong diffraction peaks corresponding to every integral value of h. The X-ray diffraction pattern of the 1-D chain, with the undiffracted beam (the $h = 0$ peak) omitted, is shown in Figure 4b.

The importance of X-ray diffraction peaks to the MJ model lies in the deep connection between part a and b of Figure 4. It is not a coincidence that each diffraction peak in Figure 4b is shown directly below an energy splitting in Figure 4a. The two phenomena arise for closely related reasons. X-ray diffraction peaks come about when the atoms in a crystal sync up with the crests of a diffraction plane wave. Because the atoms in this 1-D chain lie a units apart in x, they interfere constructively with diffraction plane waves of wavelength a ($h = \pm1$), $a/2$ ($h = \pm2$), $a/3$ ($h = \pm3$), etc. Likewise, energy splitting in the nearly free electron model arises when the atoms in a crystal sync up with the periodicity of free-electron plane waves (recall Figure 2). With the atoms in this chain a units apart in x, there are energy splittings between free-electron states of wavelength $2a$ ($k_x = \pm\pi/a$), a ($k_x = \pm2\pi/a$), $2a/3$ ($k_x = \pm3\pi/a$), etc.

What this means is that the X-ray diffraction pattern of a crystal, which is generally used to determine atomic positions, also contains information about the electronic band structure and the especially favorable valence electron counts. Let us review the MJ logic for the 1-D chain. Because the atoms are spaced a units apart in x, the strongest diffraction peaks correspond to $h = \pm1$. The atomic spacing also results in the strong mixing of free-electron plane waves of wavelength $2a$ ($k_x = \pm\pi/a$) and, consequently, an energy splitting and a gap in the density of states. If a compound adopts this structure, it likely does so in order to place its Fermi level in this gap, which would mean the nearly free electron states $\Psi_{k_x}(x)$ are filled for $-\pi/a \le k_x \le \pi/a$ and empty for all other k_x (see Figure 4a). This region of filled states is $2\pi/a$ units of reciprocal space or a single unit cell of the reciprocal lattice. It translates to one valence σ-orbital per unit cell, two valence σ-electrons per unit cell, or two valence σ-electrons per atom.

The connection between X-ray diffraction patterns and conditions for stability has been consistently used in recent studies of structure under pressure by several groups, notably Degtyareva.[93−95] The thematic underpinnings of the method are explored in a recent paper by Feng et al.[96]

4. MOVING TOWARD COMPLEXITY

As we will soon see, both the MJ model and our orbital interpretation of it hold even in much more complicated structures in 3-D space. For certain $\vec{k}$-vectors corresponding to strong X-ray diffraction peaks, there is an energy splitting between two electronic states caused by, depending on your viewpoint of choice, the mixing of two free-electron plane waves or the inherent difference between states of primarily s and p character. For very complicated band structures, however, the trick is *finding* these two electronic states, which are hidden within a large number of bands. When there are on the order of 1000 bands in a band structure, as there are for an LCAO (or plane-wave DFT) calculation of the primitive unit cell of a γ-brass superstructure with the full complement of valence orbitals, fishing out two hidden bands of interest sounds almost hopeless.

Our goal is to do just that. From a huge number of bands, we will tease out the few features that actually drive these complex crystal structures to be stable at their experimentally observed electron counts. We first demonstrate our technique on a structure that, while still not very complicated, eases the transition into 3-D space.

4.1. β'-CuZn and Its Band Structure

The first 3-D phase we discuss is β'-CuZn, an ordering of β-brass that forms at high temperatures.[97] β'-CuZn (henceforth referred to simply as CuZn) has the well-known CsCl-type

dx.doi.org/10.1021/cr1001222 |*Chem. Rev.* XXXX, XXX, 000–000

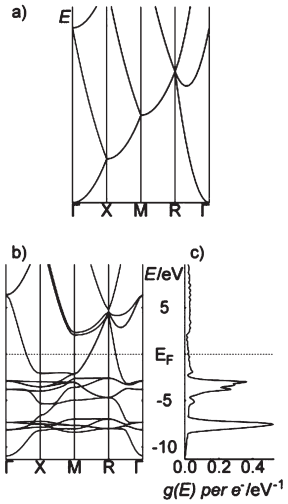

Figure 5. (a) The free-electron band structure of CsCl-type CuZn, (b) its LDA-DFT counterpart, and (c) the LDA-DFT density of states. At *k*-point M, states that are degenerate in the free-electron picture become non-degenerate in LDA-DFT, which leads to a shallow pseudogap in the density of states near the Fermi energy. The *k*-points correspond to Γ = (0, 0, 0), X = (π/a, 0, 0), M = (π/a, π/a, 0), and R = (π/a, π/a, π/a). On the energy axis of the LDA-DFT panels, the Fermi energy is defined as zero.

structure—a cubic unit cell of edge length a, with an atom of one type at (0, 0, 0) and an atom of the other type at ($a/2$, $a/2$, $a/2$). CuZn will serve as a stepping stone to the more complex Cu_5Zn_8 (γ-brass) and its relatives.

Taking the Cu and Zn 3d states to be filled core orbitals, CuZn has a valence electron count of 3/2 electrons per atom. This electron count is common among CsCl-type intermetallic phases,[98] shared by LiHg, BeCu, MgAg, MgAu, ZnAg, ZnAu, CdAg, CdAu, AlPd, AlPt, and GaNi.[99] We wish to explore the evidence for a MJ-type driving force behind this electronic trend.

The validity of the MJ model rests on the validity of the nearly free electron model. We therefore expect that a crystal structure amenable to the MJ model must have electronic states and energies resembling those of free electrons. Indeed, CuZn does. The shapes of the free-electron (Figure 5a) and LDA-DFT[100−104] (Figure 5b) electronic bands bear a striking resemblance. With the exception of the localized Zn and Cu 3d bands centered at −8 and −4 eV in Figure 5b, each band in the LDA-DFT band structure has a free-electron analog.

Of course, there are subtle differences between these two band structures. Most important to the discussion that follows is what occurs at *k*-point M = (π/a, π/a, 0). In the free-electron band structure, the four lowest-energy electronic states at *k*-point M are degenerate. They correspond to four waves of equal wavelength, $\psi_M(\vec{r}) = (1/V^{1/2})e^{i(\pi/a,\pi/a,0)\cdot\vec{r}}$, $\psi_M(\vec{r}) = (1/V^{1/2})e^{i(-\pi/a,-\pi/a,0)\cdot\vec{r}}$, $\psi_M(\vec{r}) = (1/V^{1/2})e^{i(-\pi/a,\pi/a,0)\cdot\vec{r}}$, and $\psi_M(\vec{r}) = (1/V^{1/2})e^{i(\pi/a,-\pi/a,0)\cdot\vec{r}}$, where $\vec{r}$ is the real-space position. In the LDA-DFT band structure, these states become two pairs, one degenerate and the other nearly degenerate. The pairs straddle the Fermi energy and are separated by some 4 eV.

It is not a coincidence that the Fermi energy lies within this particular energy splitting. The splitting pushes states out of the energy region from about −2 to 2 eV, which translates to a shallow pseudogap in the density of states (perhaps more easily seen in the band structure than in the DOS) that reaches a minimum close to 2 eV (Figure 5c). In the absence of a true energy gap, a compound is likely to adopt a structure that places its Fermi level in a pseudogap, as this one does. As we discuss in the next subsection, these observations of the CuZn band structure are consistent with the MJ model as traditionally implemented.

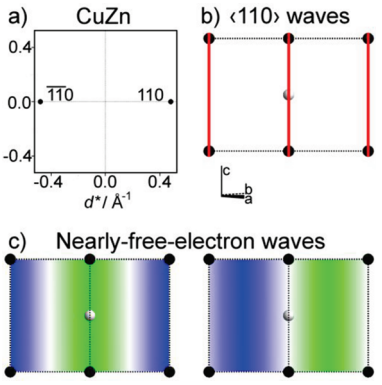

Figure 6. (a) The strongest peaks in the [1$\bar{1}$0] X-ray diffraction pattern of CuZn. (b) Crests of the ⟨110⟩ diffraction plane waves (red), with all Cu (black) and Zn (gray) atoms lying on those crests. (c) The nearly free electron states whose periodicity syncs up with the ⟨110⟩ diffraction plane waves.

4.2. What the MJ Model Has to Say About CuZn

From our earlier discussion of the 1-D chain, recall that there are two related consequences of constructive interference between crystalline ions and plane waves. One is X-ray diffraction intensity, which emerges when atoms reside on parallel Miller planes. The other is the mixing and energy splitting of free-electron states. In Figure 6, both phenomena are illustrated for CuZn.

The most intense X-ray diffraction peaks in CuZn are ⟨110⟩—the set of peaks corresponding to waves that are symmetry-equivalent to $h = 1$, $k = 1$, $l = 0$ (Figure 6a). The reason for the strength of these peaks can be seen pictorially in Figure 6b, as all Cu (black) and Zn (gray) atoms in the structure lie on successive crests of the ⟨110⟩ diffraction plane waves (red). This arrangement of atoms on parallel planes has the additional consequence of causing free-electron states to mix (Figure 6c). As shown, two free-electron states (with twice the wavelength of the ⟨110⟩ diffraction plane waves) mix to form one state whose electron density is near the ions (Figure 6c, left) and a second state whose electron density is between the ions (Figure 6c, right). Taking into account the potential of the ions, these two states split in energy.

To fully appreciate what the MJ model says about CuZn, consider where the states in Figure 6c reside in the band structures in Figure 5. These two states are a mixture of the free-electron plane waves $\psi_M(\vec{r}) = (1/V^{1/2})e^{i(\pi/a,\pi/a,0)\cdot\vec{r}} = (1/V^{1/2})e^{i(\pi/a)(x+y)}$ and $\psi_M(\vec{r}) = (1/V^{1/2})e^{i(-\pi/a,-\pi/a,0)\cdot\vec{r}} = (1/V^{1/2})e^{-i(\pi/a)(x+y)}$, which are found at *k*-point M = (π/a, π/a, 0) in the band structures. After mixing, these wave functions resemble $\Psi_M(\vec{r}) = [1/(2V)^{1/2}](e^{i(\pi/a)(x+y)} + e^{-i(\pi/a)(x+y)}) = (2/V)^{1/2}\cos[(\pi/a)(x+y)]$ (Figure 6c, left) and $\Psi_M(\vec{r}) = -[i/(2V)^{1/2}](e^{i(\pi/a)(x+y)} - e^{-i(\pi/a)(x+y)}) = (2/V)^{1/2}\sin[(\pi/a)(x+y)]$ (Figure 6c, right). Not shown in Figure 6 are another pair of states, also at *k*-point M, corresponding to the $\bar{1}$10 diffraction plane wave. After mixing, they resemble the functions $\Psi M(\vec{r}) = (2/V)^{1/2}\cos[(\pi/a)(-x+y)]$ and $\Psi_M(\vec{r}) = (2/V)^{1/2}\sin[(\pi/a)(-x+y)]$.

We can now rationalize our earlier observations of the band structure of CuZn (Figure 5). At *k*-point M, four degenerate free-electron states $(1/V^{1/2})e^{i(\pi/a)(x+y)}$, $(1/V^{1/2})e^{-i(\pi/a)(x+y)}$,

dx.doi.org/10.1021/cr1001222 |*Chem. Rev.* XXXX, XXX, 000–000

$(1/V^{1/2})e^{i(\pi/a)(-x+y)}$, and $(1/V^{1/2})e^{-i(\pi/a)(-x+y)}$) mix to form four nearly free electron states $\{(2/V)^{1/2}\cos[(\pi/a)(x+y)]$, $(2/V)^{1/2}\sin[(\pi/a)(x+y)]$, $(2/V)^{1/2}\cos[(\pi/a)(-x+y)]$, and $(2/V)^{1/2}\sin[(\pi/a)(-x+y)]\}$. The latter four states come in two pairs, one of which has its electron density near the ions and the other of which has its electron density between the ions. This leads to an energy splitting, made possible by the same arrangement of atoms on parallel planes that also results in strong ⟨110⟩ X-ray diffraction peaks. The energy splitting (Figure 5b) in turn leads to the pseudogap (and stable valence electron count around 3/2 electrons per atom) in Figure 5c.

Before moving on, one more point should be clarified. In order to be formally correct about the mixing of these free-electron states $[(1/V^{1/2})e^{i(\pi/a)(x+y)}$, $(1/V^{1/2})e^{-i(\pi/a)(x+y)}$, $(1/V^{1/2})e^{i(\pi/a)(-x+y)}$, and $(1/V^{1/2})e^{-i(\pi/a)(-x+y)}]$, one would have to consider all four to mix together, rather than pairwise. However, the pairwise mixing we have illustrated, in addition to being easier to visualize, is qualitatively accurate. Strong energy splitting of free-electron states can occur only when the states are separated by a reciprocal lattice vector, corresponding to a significant Fourier component (i.e., a strong X-ray diffraction peak), as this creates states whose electron density is either near or between ions. Because CuZn has strong ⟨110⟩ peaks, the states corresponding to $(\pi/a, \pi/a, 0)$ and $(-\pi/a, -\pi/a, 0)$ mix strongly, as do those corresponding to $(-\pi/a, \pi/a, 0)$ and $(\pi/a, -\pi/a, 0)$. However, because the ⟨100⟩ peaks are nearly absent (they would be formally absent if Cu and Zn atoms were identical and/or randomly mixed in the structure), other pairs of these free-electron states do not mix strongly. Our pairwise picture is therefore qualitatively accurate for CuZn.[105]

4.3. Finding Hidden Plane Waves in CuZn

The evidence in the previous subsection is all consistent with the MJ model for CuZn. However, all of the evidence is indirect. Without actually performing a calculation that allows us to look at the electronic states in CuZn, we cannot really prove that the splitting of free-electron waves is driving the stability of the valence electron count. The chemical reality of this system, as it turns out, is not quite as clean as the plane-wave story presented above.

In examining the electronic structure of CuZn more closely, we again employ eH theory as the simplest LCAO model. This method is both computationally cheap and chemically transparent, expressing crystalline electronic states as LCAO whose energies are shaped by bonding and antibonding interactions. The drawback of the extended Hückel implementation of LCAO is that, if one is not careful in choosing atomic parameters, the results of an LCAO calculation may bear little resemblance to more quantitatively reliable calculations. For this reason, we calibrate the LCAO parameters of Cu and Zn to match the LDA-DFT band structure of CuZn, using an automated optimization procedure to find the best fit. This method has proven reliable in the past.[8,17,68,106−108]

The LDA-DFT and LCAO band structures of CuZn are superimposed in Figure 7, with the Fermi energy defined as zero in both. For the bands that are filled, the LCAO bands (green) match their LDA-DFT counterparts (black) quite well. This suggests that these LCAO parameters represent the chemical reality of the system as accurately as possible. The calibrated atomic parameters for the Slater-type orbitals in this calculation are H_{ii}(Cu 4s) = −11.63 eV, ζ_s = 1.80; H_{ii}(Cu 4p) = −5.72 eV, ζ_p = 1.625; H_{ii}(Cu 3d) = −11.94 eV, $\zeta_{1,d}$ = 6.93, $\zeta_{2,d}$ = 2.02, $c_{1,d}$ = 0.7234, $c_{2,d}$ = 0.7962; H_{ii}(Zn 4s) = −12.71 eV, ζ_s = 1.92; H_{ii}(Zn 4p) = −7.84 eV, ζ_p = 1.55; H_{ii}(Zn 3d) = −15.95 eV, $\zeta_{1,d}$ = 6.82, $\zeta_{2,d}$ = 2.26, $c_{1,d}$ = 0.7582, $c_{2,d}$ = 0.5730. These parameters will be used for the remainder of our discussion of CuZn.

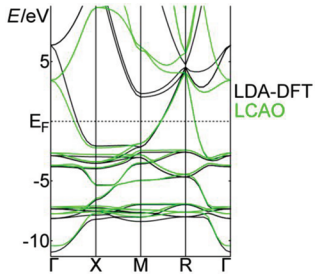

Figure 7. The band structure of CuZn, calculated using LDA-DFT methods (black) and LCAO methods with atomic parameters calibrated to the LDA-DFT band structure (green). For bands that are filled, the energies calculated by the two methods are quite close. For both methods, the Fermi energy is defined as zero.

Armed with a quantitatively accurate band structure calculation that allows us to view the electronic states of CuZn as linear combinations of atomic orbitals, we are ready to search for the wavelike electronic states on which the MJ model focuses. In the earlier case of the 1-D chain, comparison between the nearly free electron (Figure 2) and LCAO (Figure 3) band structures was straightforward because each individual LCAO crystal orbital had an obvious wave analog. The case is not quite so simple for real 3-D structures. Each nearly free electron wavelike state, rather than having a single LCAO crystal orbital analog, is mixed into many LCAO states. If we wish to use an LCAO calculation to confirm, rather than simply infer, the validity of the MJ model for real chemical structures, we must develop a strategy to break down an LCAO band structure into its relevant plane waves. We do so in this subsection.

The difference between nearly free electron and LCAO electronic states is largely a matter of basis set—the former are sums of plane waves, while the latter are sums of atomic valence orbitals. In principle, the two basis sets can be interconverted. That is, plane waves can be expressed as sums of valence orbitals, and vice versa. Our strategy is outlined as follows: (1) express the states in a nearly free electron MJ band as sums of LCAO crystal orbitals, (2) assign energies to those nearly free electron states as weighted averages of the LCAO energies, and (3) plot the energy of the MJ band hidden within the structure. In this way, we can start with a complicated LCAO band structure and tease out the information relevant to the MJ model.

Free-electron plane-wave states have the form $\psi_{\vec{k}}(\vec{r}) = (1/V^{1/2})e^{i\vec{k}\cdot\vec{r}}$. Nearly free electron states $\Psi_{\vec{k}}(\vec{r})$ are mixtures of these plane waves. The translational symmetry of a crystal dictates that mixing can only occur between waves separated by a reciprocal lattice vector $\vec{G}$:

$$\Psi_{\vec{k}}(\vec{r}) = \frac{1}{\sqrt{V}}\sum_{\vec{G}} c_{\vec{G},\vec{k}}\, e^{i(\vec{k}+\vec{G})\cdot\vec{r}}$$

The $c_{\vec{G},\vec{k}}$ are complex coefficients of each component of the nearly free electron state. As the nearly free electron model requires that deviation from free-electron states is small, the dominant component of each state (i.e., the one with the largest magnitude $c_{\vec{G},\vec{k}}$) is the one corresponding to $\vec{G}$ = (0, 0, 0).

Each normalized nearly free electron state $\Psi_{\vec{k}}(\vec{r})$ is then expressed, as accurately as possible,[109] as a linear combination of

dx.doi.org/10.1021/cr1001222 |Chem. Rev. XXXX, XXX, 000–000

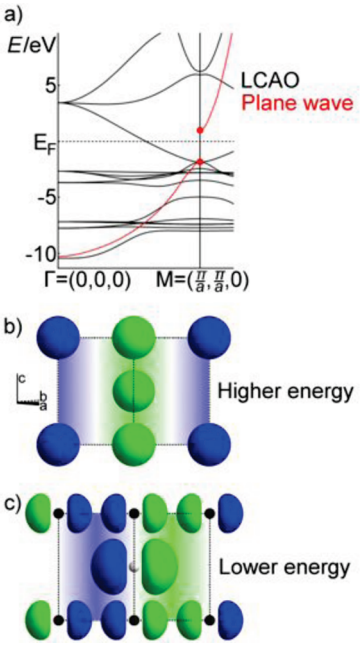

Figure 8. (a) The LCAO band structure of CuZn (black) and the projected nearly free electron MJ band (red), plotted along a straight path through k-space from $\Gamma = (0, 0, 0)$ through $M = (\pi/a, \pi/a, 0)$. (b, c) The two projected crystal orbitals at M, expressed as contours of their component s and p atomic orbitals, with the corresponding nearly free electron waves shown lightly in the background. The energies of these two states straddle the Fermi energy.

the full set of normalized LCAO wave functions $\Phi_{i,\vec{k}}(\vec{r})$ at the same k-point:

$$\Psi_{\vec{k}}(\vec{r}) = \sum_i p_{i,\vec{k}} \Phi_{i,\vec{k}}(\vec{r})$$

The coefficients p_i in the above equation are projections of the nearly free electron state onto each LCAO wave function:

$$p_{i,\vec{k}} = \int_{\text{unit cell}} \Psi_{\vec{k}}(\vec{r}) \Phi_{i,\vec{k}}{}^*(\vec{r})\, dV$$

In the second step of the process, an energy $\varepsilon(\vec{k})$ is assigned to each nearly free electron state $\Psi_{\vec{k}}(\vec{r})$. The energy is taken to be the weighted average of the energies $\varepsilon_{i,\vec{k}}$ of the constituent LCAO crystal orbitals:

$$\varepsilon(\vec{k}) = \frac{\sum_i \varepsilon_{i,\vec{k}} |p_{i,\vec{k}}|^2}{\sum_i |p_{i,\vec{k}}|^2}$$

The final step is to plot the energy of the projected MJ band. Recalling that the significant feature of this plot (an energy splitting that corresponds to the strong ⟨110⟩ X-ray diffraction peaks) is expected at k-point $M = (\pi/a, \pi/a, 0)$, this plot is constructed along a straight path from $\vec{k} = (0, 0, 0)$ through $\vec{k} = (\pi/a, \pi/a, 0)$. However, we must first take a brief step back and explain how the coefficients $c_{\vec{G},\vec{k}}$ are determined.

In principle, each nearly free electron state $\Psi_{\vec{k}}(\vec{r})$ is the sum of an infinite number of plane-wave terms. Fortunately, very few of these terms make a significant contribution. A plane wave whose reciprocal lattice vector $\vec{G}$ corresponds to an intense X-ray diffraction peak mixes strongly into the sum only if its energy is similar to that of the dominant $\vec{G} = (0, 0, 0)$ term—that is, if $|\vec{k} + \vec{G}| \approx |\vec{k}|$. For most of our path through k-space—all but a small range close to $\vec{k} = (\pi/a, \pi/a, 0)$—there is no term close in energy to the $\vec{G} = (0, 0, 0)$ term. Thus, far from $\vec{k} = (\pi/a, \pi/a, 0)$, the nearly free electron states approach $\Psi_{\vec{r}}(\vec{r}) = (1/V^{1/2})e^{i\vec{k}\cdot\vec{r}}$.

The situation is different close to $\vec{k} = (\pi/a, \pi/a, 0)$. The $\vec{G} = (0, 0, 0)$ and $\vec{G} = (-2\pi/a, -2\pi/a, 0)$ terms become close in energy, which means the nearly free electron states must be expressed as $\Psi_{\vec{k}}(\vec{r}) = (1/V^{1/2})(c_1 e^{i\cdot\vec{k}\cdot\vec{r}} + c_2 e^{i(\vec{k}+(-2\pi/a,-2\pi/a,0))\cdot\vec{r}})$. On the "near" side of $\vec{k} = (\pi/a, \pi/a, 0)$ [at $\vec{k} = (0.99\pi/a, 0.99\pi/a, 0)$, say], the $\vec{G} = (-2\pi/a, -2\pi/a, 0)$ term is higher in energy than the dominant term. We therefore expect this mixing to push the state to a lower energy, and we choose the c_1 and c_2 that result in the lowest energy. On the "far" side of $\vec{k} = (\pi/a, \pi/a, 0)$ [at $\vec{k} = (1.01\pi/a, 1.01\pi/a, 0)$, say], the reverse is true. The $\vec{G} = (-2\pi/a, -2\pi/a, 0)$ term is lower in energy than the dominant term and pushes the state up in energy. We choose the c_1 and c_2 that result in the highest energy.

In Figure 8a, the projected MJ band (red) is plotted on top of the calibrated LCAO band structure (black), with a satisfying result. The MJ band resembles a nearly free electron parabola, with an energy splitting of 2.74 eV at $M = (\pi/a, \pi/a, 0)$, the k-point corresponding to the strong ⟨110⟩ X-ray diffraction peaks. The two projected states at M (red circles at −1.80 and 0.94 eV) straddle the Fermi energy, further suggesting that the splitting does indeed help to stabilize CuZn at 3/2 valence electrons per atom.

These two projected states at M are shown in Figure 8b,c as contours of their component s and p atomic orbitals.[110] Both states resemble their nearly free electron wave analogs, shown lightly in the background. The higher-energy state (Figure 8b) is primarily a combination of s orbitals, and the lower-energy state (Figure 8c) a combination of p orbitals. This ordering is representative of the inverted region, as defined earlier for a 1-D system. Though the ordering could have been reversed for different atomic or unit cell parameters, the energy splitting in the projected band would have been present regardless.

In contrast to Figure 8, which focuses on the wavelike character of the projected states at M, Figure 9 examines their local atomic orbital interactions. The projected states are shown from a viewpoint slightly offset from our usual one, from which

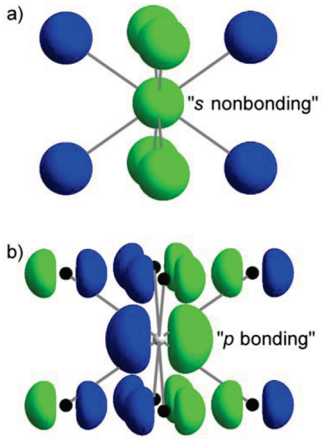

Figure 9. The local atomic orbital interactions of a Zn atom and its nearest neighbors in the (a) higher- and (b) lower-energy projected MJ states of CuZn at $M = (\pi/a, \pi/a, 0)$. The higher-energy state is primarily a nonbonding combination of s orbitals, while the lower-energy state is primarily a bonding combination of p orbitals.

dx.doi.org/10.1021/cr1001222 |Chem. Rev. XXXX, XXX, 000–000

we can see a Zn atom and its cube of eight nearest-neighboring Cu atoms. In the higher-energy state (Figure 9a), the central atom interacts with four of its neighbors in a σ-bonding manner and four in a σ-antibonding manner, resulting in a roughly nonbonding crystal orbital. In the lower-energy state (Figure 9b), the central atom interacts with four of its neighbors in a π-bonding manner and four in an approximately nonbonding manner, resulting in a bonding crystal orbital. The corresponding pictures showing the local coordination of a Cu atom would look almost identical.

4.4. Energy Splitting at Other *k*-Points in CuZn

While the projected band, its energy splitting, and its wavelike LCAO states in Figure 8 further support the MJ view of CuZn, they should still be met with a healthy dose of skepticism. One shortcoming of the argument presented in the previous subsection is that it examines the energy splitting of the projected MJ band at only one *k*-point, M = (π/a, π/a, 0). If such splittings were found only at individual isolated *k*-points, then they would lead to a negligible pseudogap in the density of states. In order to argue that such splittings lead to a substantial pseudogap, we must show that they occur at a continuum of *k*-points.

At which *k*-points should we expect to find these energy splittings? Recall that in order for two plane-wave electronic states $\psi_{\vec{k}_1}(\vec{r}) = (1/V^{1/2})e^{i\vec{k}_1\cdot\vec{r}}$ and $\psi_{\vec{k}_2}(\vec{r}) = (1/V^{1/2})e^{i\vec{k}_2\cdot\vec{r}}$ to mix and split, they must be separated by a reciprocal lattice vector $\vec{G}$ and be of equal energy. In symbols, these two conditions become

$$\vec{k}_1 + \vec{G} = \vec{k}_2$$

$$|\vec{k}_1| = |\vec{k}_2|$$

In order for the resulting energy splitting to be large, there is the additional requirement that $\vec{G}$ correspond to a strong X-ray diffraction peak. As the strongest peaks for CuZn are ⟨110⟩, $\vec{G}$ can be any permutation of $\pm 2\pi/a$, $\pm 2\pi/a$, and 0. This ensures that once $\psi_{\vec{k}_1}(\vec{r})$ and $\psi_{\vec{k}_2}(\vec{r})$ mix, one wave function has its electron density concentrated near the ions and the other between the ions.

Certainly, $\vec{k}_1 = (\pi/a, \pi/a, 0)$ and $\vec{k}_2 = (-\pi/a, -\pi/a, 0)$ satisfy these conditions. These vectors represent the two waves whose splitting is shown in Figure 8. However, the coordinates of $\vec{k}_1$ and $\vec{k}_2$ need not be such round numbers. Consider the more general vectors $\vec{k}_1 = (\pi/a + \alpha, \pi/a - \alpha, \beta)$ and $\vec{k}_2 = (-\pi/a + \alpha, -\pi/a - \alpha, \beta)$, for any values of α and β. They too satisfy all of the above conditions for large energy splitting. The two degrees of freedom, α and β, indicate that *splitting occurs not just at isolated k-points, but on 2-D planes of k-points*. This idea has been discussed in previous literature, in the language of mixing of charge-density waves. In such terms, the vectors $\vec{G}$ separating parallel planes in reciprocal space are known as Fermi surface nesting vectors.[81,111]

In the reciprocal space of CuZn, there are 12 planes that satisfy the conditions for large energy splitting. These planes intersect to form the polyhedron in Figure 10a. The polyhedron constructed in this way is often called the Jones zone and is in this case equivalent to the first Brillouin zone of the bcc structure. To a first approximation, the Jones zone can be used to estimate the likely electron count for β-brass alloys and CsCl-type intermetallics. The nearly free electron states $\Psi_{\vec{k}}(\vec{r})$ inside the zone lie below the energy splitting and are filled, while those outside the zone lie above the energy splitting and are empty. The reciprocal-space volume of the Jones zone thus represents the number of filled valence orbitals per unit cell. The volume in this case is

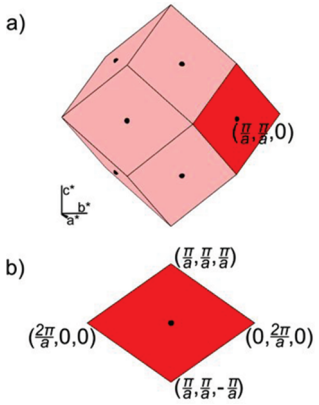

Figure 10. (a) The surface that separates the CuZn nearly free electron states that are above the energy splitting (outside the Jones zone) from those that are below it (inside the Jones zone). (b) One face of the Jones zone, symmetry-equivalent to all the others.

$2(2\pi/a)^3$ or two unit cells of the reciprocal lattice. This translates to two filled valence orbitals per unit cell, four valence electrons per unit cell, or two valence electrons per atom.

While this estimate is in the right ballpark (though significantly higher than Hume-Rothery's observation of 3/2 valence electrons per atom for β-brass), the argument used to derive it has a notable flaw. Namely, the surface in Figure 10a is not a sphere. It has some points that jut out farther from the origin than others. Because the energy of a plane-wave electronic state is proportional to $|\vec{k}|^2$, splitting occurs at a higher energy for those *k*-points that are farther out. It is therefore possible that the top of the splitting at (for example) $\vec{k} = (\pi/a, \pi/a, 0)$ is lower in energy than the bottom of the splitting at (for example) $\vec{k} = (2\pi/a, 0, 0)$. This possibility must be explored, as it would argue against the above assumption that states are filled if and only if they lie inside the Jones zone.

We therefore calculate the energies at the top and bottom of the splitting over the entire polyhedral surface. Only one of the 12 symmetry-equivalent faces (Figure 10b) need be calculated. The result is shown in Figure 11a. As expected, the energy curves of both the top (gray) and bottom (black) of the splitting resemble paraboloids with respect to $\vec{k}$. We see that our concern was justified—the top of the splitting at $\vec{k} = (\pi/a, \pi/a, 0)$ is indeed lower in energy than the bottom of the splitting at $\vec{k} = (2\pi/a, 0, 0)$. As a result, the Fermi energy (red) cannot lie within the gap for all *k*-points on the Jones zone surface simultaneously.

In the absence of a true energy gap between the top and bottom paraboloids in Figure 11a, the Fermi energy is likely to be found in a pseudogap. One might reasonably guess that such a pseudogap would be centered at an energy that lies within the splitting for most of the Jones zone surface. Translated into the language of Figure 11a, the "ideal" number of electrons for this system would place the Fermi energy (red plane) between the gray and black paraboloids for as much of the illustrated area of reciprocal space as possible. By inspection, this is accomplished when the Fermi energy just touches the bottom of the gray paraboloid, 0.94 eV above the actual Fermi energy. This estimate is confirmed in Figure 11b. Integrating the density of states up to this energy predicts that the "ideal" electron count for CuZn is 1.77 valence electrons per atom.

Of course, there are several caveats to the electron count at which the previous paragraph arrives. The first is that our

dx.doi.org/10.1021/cr1001222 |*Chem. Rev.* XXXX, XXX, 000–000

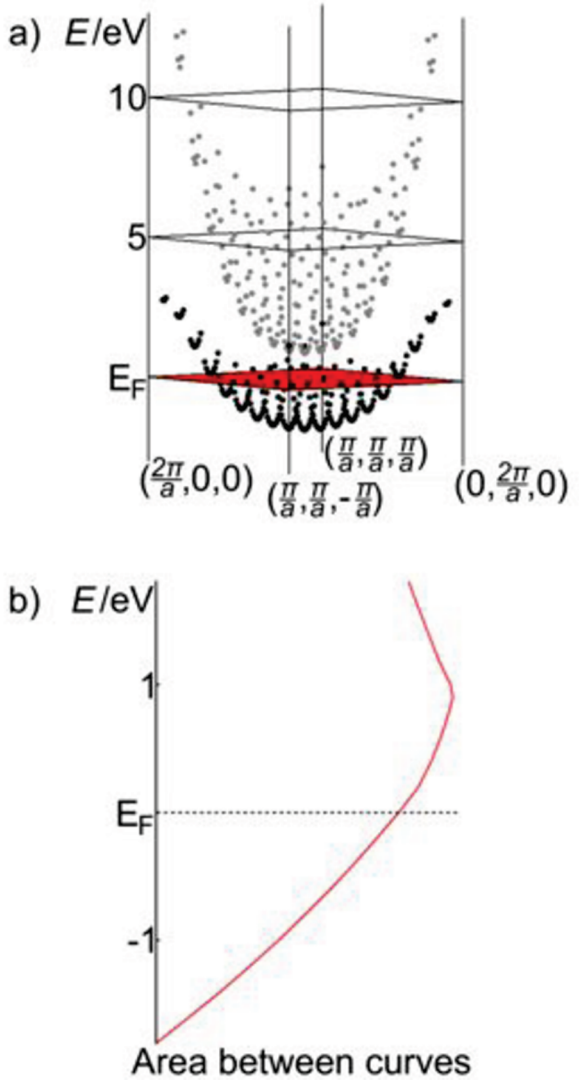

Figure 11. (a) The energies at the top (gray) and bottom (black) of the splitting on one face of the Jones zone. (b) The area on the face for which a given energy lies between the two paraboloids. Area is plotted in arbitrary units.

definition of "ideal" says little of how well the structure competes with others. Whether a structure forms at a given electron count depends not only on its own electronic properties, but on those of all competing structures. So even if CsCl-type CuZn has a pseudogap that favors 1.77 valence electrons per atom, it might have to compete with other possible structures that favor the same electron count. Second, the exact placement of this "ideal" electron count is not general for CsCl-type compounds and depends on the atomic and unit cell parameters. For example, if the energy splitting in Figure 11a were wider, the "ideal" electron counts would move closer to 2. The third caveat is that the pseudogap in CuZn is not very deep. Because the Jones zone (Figure 10a) has vertices that jut out sharply, the top and bottom of the energy splitting (Figure 11a) are not fully separated.

Mott and Jones, in their analysis of the β-brass structure, adopted a slightly different criterion for determining the "magic" electron count. Rather than assuming electrons fill a polyhedron, as we do (Figure 10a), they assumed electrons fill the inscribed sphere.[41,42] Their method leads to an electron count of 1.48 valence electrons per atom. As our discussion shows, there is no unique way to define the "optimum" filling—only a range of electron counts. The literature following Mott and Jones has discussed at some length the effects of subtly different electron fillings relative to the polyhedron we use.[43] The question becomes even more subtle when one considers that thermodynamic stability must be judged relative to other possible structures. As the relative stabilities of metallic crystal structures have been captured using Hückel theory,[112] we suspect they are also within the scope of our reasoning.

This concludes our discussion of CuZn, with reasonable results but an interesting and real ambiguity. We have adapted the MJ model to chemical ways of looking at the electronic structure of extended systems and confirmed the observed range of stability between 1 and 2 valence electrons per atom in β-brass alloys and CsCl-type intermetallics. However, it emerges that for this particular structure, the "ideal" electron count is imprecise and element-dependent. As the remainder of this work will show, increasing complexity can actually sharpen an intermetallic structure's preference for a particular electron count.

5. CRYSTAL STRUCTURES OF THE γ-BRASSES

At a slightly higher Zn concentration than β-brass lies γ-brass. The γ-brass region of the Cu−Zn phase diagram includes the ordered intermetallic Cu_5Zn_8.[3] Taking the Cu and Zn 3d states to be filled-core orbitals, Cu_5Zn_8 has a valence electron count of 21/13 electrons per atom. Cu_5Zn_8 has a considerably more complex structure than CuZn. It is worth noting, however, that the two are related. The atomic positions of a $3 \times 3 \times 3$ supercell of CuZn with vacancies at its vertices and center differ from those of Cu_5Zn_8 only by small distortions. Crystallizing with $I\bar{4}3m$ symmetry, the cubic unit cell of Cu_5Zn_8 is traditionally seen as a body-centered arrangement of two identical 26-atom clusters. These clusters, termed γ-brass clusters, are in no way chemically isolated and "exist" only as visual mnemonics.

A γ-brass cluster can be viewed in a number of ways. Perhaps the most common view (Figure 12a) is of four nested polyhedra, one for each crystallographically inequivalent site. From the cluster center to the periphery, these polyhedra are an inner tetrahedron (IT), an outer tetrahedron (OT), an octahedron (OH), and a cuboctahedron (CO). An alternative view (Figure 12b), more suggestive of the experimental site preferences, connects the OT and OH sites (Cu atoms in Cu_5Zn_8) as an adamantane-like cage and the IT and CO sites (Zn atoms in Cu_5Zn_8) as a tetrahedron of tetrahedra.[17,113] The full 52-atom cubic unit cell of Cu_5Zn_8 is shown in Figure 12c.

Cu_5Zn_8 is the parent structure of a number of even more complicated superstructures, which we call $2 \times 2 \times 2$ γ-brasses. As suggested by the name, these compounds have cubic unit cells that resemble the Cu_5Zn_8 unit cell doubled in all three dimensions. Each of these superstructures differs from Cu_5Zn_8 by some combination of distortions, colorings, vacancies, and interstitial atoms. Among the $2 \times 2 \times 2$ γ-brasses that have been solved using single crystal X-ray diffraction are $Zn_{21}Pt_5$,[18,33] $Li_{21}Si_5$,[27,28] $Mg_{44}Rh_7$,[20] $Mg_{44}Ir_7$,[19] Na_6Tl,[21] Mg_6Pd,[22] $Cu_{41}Sn_{11}$,[23,24] $Sm_{11}Cd_{45}$,[25] $Zn_{39}Fe_{11}$,[26] $Al_{69}Ta_{39}$,[29] $Zn_{13}(Fe,Ni)_2$,[30] $Mg_{29}Ir_4$,[31] $Zn_{20.44}Mo$,[32] $Zn_{91}Ir_{11}$,[34] and $Li_{13}Na_{29}Ba_{19}$.[35] All of these structures crystallize with $F\bar{4}3m$ symmetry. As the Cu_5Zn_8 unit cell contains two γ-brass clusters and its superstructures represent a doubling of the unit cell in all three dimensions, each unit cell contains 16 similar clusters and roughly 400 atoms.

dx.doi.org/10.1021/cr1001222 |Chem. Rev. XXXX, XXX, 000–000

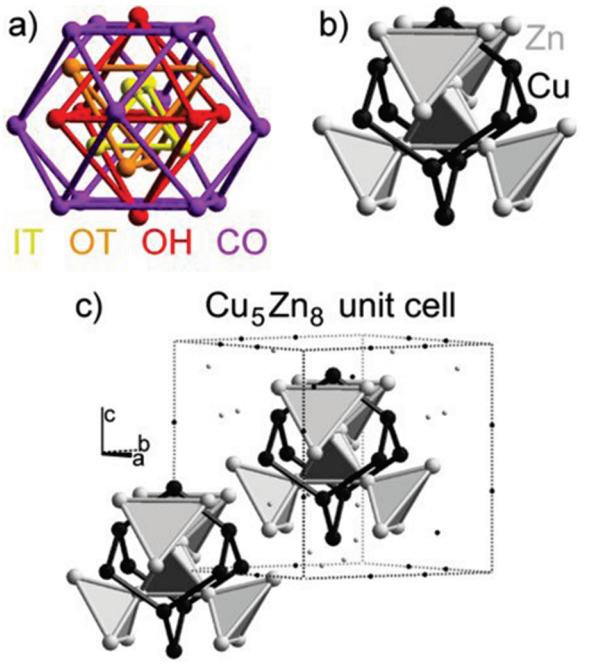

Figure 12. (a) One view of a γ-brass cluster, showing an inner tetrahedron (IT, yellow), an outer tetrahedron (OT, orange), an octahedron (OH, red), and a cuboctahedron (CO, purple). (b) A second view, more suggestive of the site preferences in Cu_5Zn_8, showing an adamantane-like cage (Cu atoms, black) and a tetrahedron of tetrahedra (Zn atoms, gray). (c) The cubic unit cell of Cu_5Zn_8, emphasizing its body-centered arrangement of γ-brass clusters.

We wish to use MJ reasoning as the starting point for our analysis of the γ-brasses. This requires knowledge of which X-ray diffraction peaks are most intense. The strongest peaks in Cu_5Zn_8 are ⟨330⟩ and ⟨114⟩ (Figure 13a). While the relative intensities vary from system to system, the strongest peaks in $2 \times 2 \times 2$ γ-brasses are generally ⟨660⟩, ⟨228⟩, and ⟨555⟩ (Figure 13b). There is an interesting story to be told about the structural source of these strongest X-ray peaks. However, to avoid interrupting this work with a lengthy diversion, we simply take these diffraction patterns as given for now and save the full diffraction pattern story for the Appendix.

6. REINTERPRETING THE MJ MODEL OF Cu_5Zn_8

The MJ model has long been the dominant theoretical rationale for Hume-Rothery's empirical observations of the phase stability of γ-brass. According to the model, the alignment of atoms with ⟨330⟩ and ⟨114⟩ plane waves splits the energies of the corresponding nearly free electron states. Together, the energy splittings create a pseudogap in the density of states, stabilizing the crystal structure for a narrow range surrounding the experimental electron count of Cu_5Zn_8, 21/13 valence electrons per atom. To gain a more chemical understanding of this electron-counting rule, we now use the machinery developed in our earlier discussion of CuZn to reinterpret the MJ arguments for Cu_5Zn_8 in terms of LCAO.

6.1. The Band Structure of Cu_5Zn_8 γ-Brass

MJ reasoning rests on the nearly free electron model. As Cu_5Zn_8 has proven amenable to the MJ model, we expect its band structure to resemble that of free electrons. The

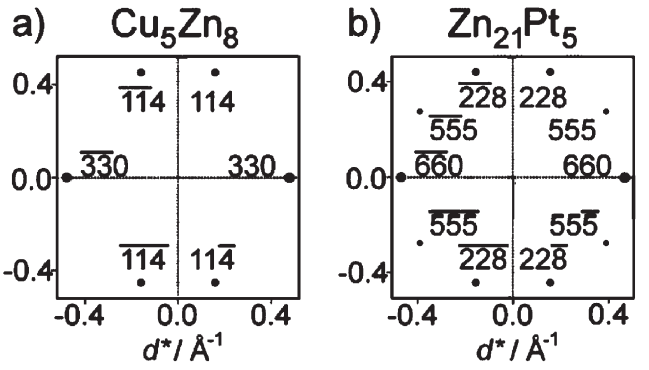

Figure 13. The strongest peaks in the $[1\bar{1}0]$ X-ray diffraction patterns of (a) Cu_5Zn_8 and (b) $Zn_{21}Pt_5$, a $2 \times 2 \times 2$ γ-brass.

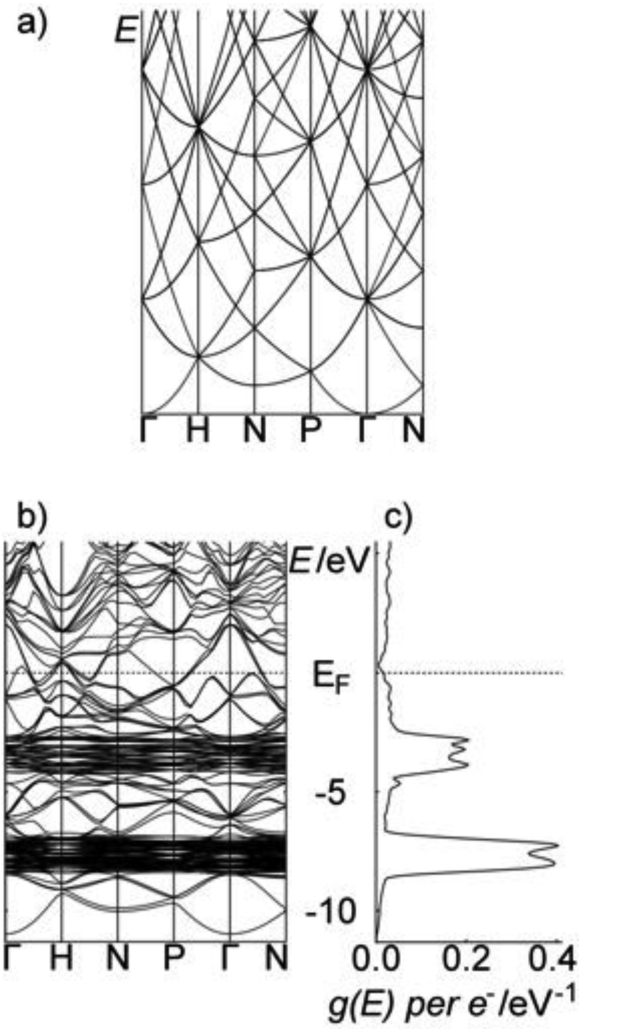

Figure 14. (a) The free-electron band structure of Cu_5Zn_8, (b) its LDA-DFT counterpart, and (c) the LDA-DFT density of states. Note the pseudogap in the density of states near the Fermi energy. The k-points with respect to the cubic cell correspond to $\Gamma = (0, 0, 0)$, $H = (2\pi/a, 0, 0)$, $N = (\pi/a, \pi/a, 0)$, and $P = (\pi/a, \pi/a, \pi/a)$. On the energy axis of the LDA-DFT panels, the Fermi energy is defined as zero.

resemblance, however, is more difficult to confirm by inspection for Cu_5Zn_8 (Figure 14) than it was for CuZn (Figure 5).

dx.doi.org/10.1021/cr1001222 |*Chem. Rev.* XXXX, XXX, 000–000

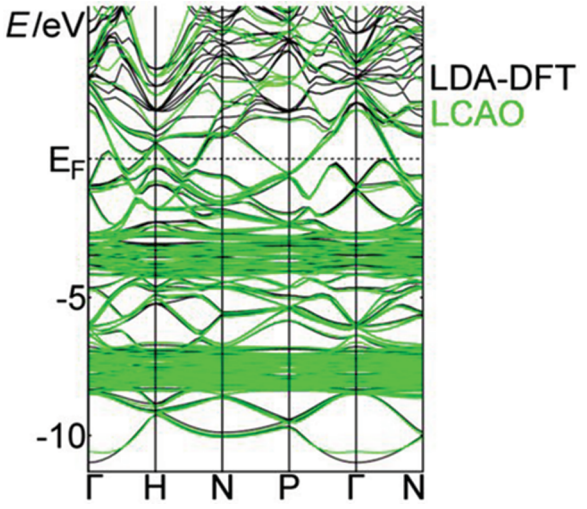

Figure 15. The band structure of Cu_5Zn_8, calculated using LDA-DFT methods (black) and LCAO methods with atomic parameters calibrated to the LDA-DFT band structure (green). For bands that are filled, the energies calculated by the two methods are quite close. For both methods, the Fermi energy is defined as zero.

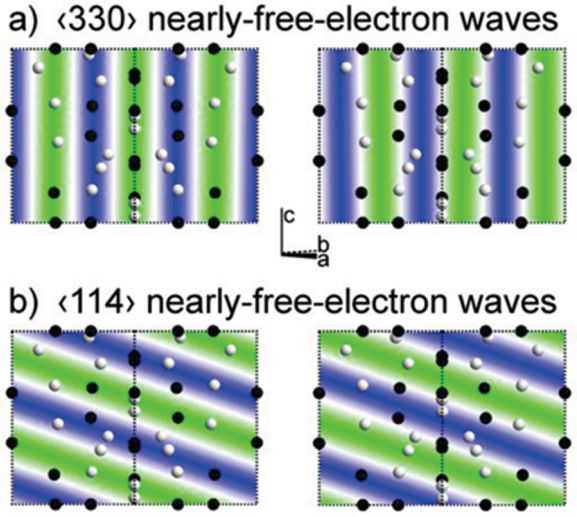

Figure 16. The nearly free electron states whose periodicity syncs up with the (a) ⟨330⟩ and (b) ⟨114⟩ diffraction plane waves of Cu_5Zn_8. Cu (black) and Zn (gray) atoms are shown.

The 26-atom primitive unit cell of Cu_5Zn_8 produces quite a complicated picture, in which it is somewhat difficult to pick out the individual parabolas. With some effort, though, one can see similarities in the shapes of the free-electron (Figure 14a) and LDA-DFT[100−104] (Figure 14b) bands, especially below the Fermi energy. Excluding the regions of localized Zn and Cu 3d bands centered at −8 and −4 eV, each band in the LDA-DFT band structure has a free-electron analog.

The density of states of Cu_5Zn_8 (Figure 14c) shows the hallmark of an electron phase: a pseudogap very close to the Fermi energy. This pseudogap, centered just above the Fermi energy, is more pronounced than the corresponding pseudogap in CuZn (Figure 5c).

In order to examine the source of this pseudogap and its relative sharpness, we again turn to LCAO. To ensure the quantitative accuracy of our LCAO calculation of Cu_5Zn_8, we calibrate the Cu and Zn atomic parameters to match LDA-DFT. These two band structures are superimposed in Figure 15, with the Fermi energy defined as zero in both. The close match between LCAO (green) and LDA-DFT (black) suggests that these LCAO parameters accurately represent the chemical reality of the system. The calibrated atomic parameters for the Slater-type orbitals in this calculation are H_{ii}(Cu 4s) = −11.47 eV, ζ_s = 1.75; H_{ii}(Cu 4p) = −5.55 eV, ζ_p = 1.69; H_{ii}(Cu 3d) = −11.95 eV, $\zeta_{1,d}$ = 6.09, $\zeta_{2,d}$ = 2.00, $c_{1,d}$ = 0.6006, $c_{2,d}$ = 0.6873; H_{ii}(Zn 4s) = −12.57 eV, ζ_s = 1.88; H_{ii}(Zn 4p) = −7.53 eV, ζ_p = 1.48; H_{ii}(Zn 3d) = −16.02 eV, $\zeta_{1,d}$ = 6.04, $\zeta_{2,d}$ = 2.21, $c_{1,d}$ = 0.6161, $c_{2,d}$ = 0.5730. Not surprisingly, these parameters, which will be used for the remainder of our discussion of Cu_5Zn_8, are very similar to those used for CuZn.

6.2. Finding Hidden Plane Waves in Cu_5Zn_8

The strength of the ⟨330⟩ and ⟨114⟩ X-ray diffraction peaks indicates that the atoms in Cu_5Zn_8 sync up with the corresponding sets of Miller planes. According to the MJ model, this periodic arrangement of ions causes free-electron plane-wave electronic states (with twice the wavelength of the diffraction plane waves) to mix and split in energy. The result, as we saw in our earlier discussion of CuZn, is pairs of nearly free electron states in which one has its electron density near the ions and the other between the ions.

Though the atoms in Cu_5Zn_8 are not as neatly aligned on diffraction planes as those in CuZn, the expected wavelike states (Figure 16) are qualitatively the same. Figure 16a shows a mixing representative of the ⟨330⟩ X-ray diffraction peaks. These two states are a mixture of the plane waves $\psi_N(\vec{r}) = (1/V^{1/2})e^{i(3\pi/a,3\pi/a,0)} = (1/V^{1/2})e^{i(3\pi/a)(x+y)}$ and $\psi_N(\vec{r}) = (1/V^{1/2})e^{i(-3\pi/a,-3\pi/a,0)} = e^{-i(3\pi/a)(x+y)}$, which are found at k-point N = $(\pi/a, \pi/a, 0)$ with respect to the cubic unit cell. After mixing, these wave functions resemble $\Psi_N(\vec{r}) = [1/(2V)^{1/2}](e^{i(3\pi/a)(x+y)} + e^{-i(3\pi/a)(x+y)}) = (2/V)^{1/2}\cos[3\pi/a(x+y)]$ (Figure 16a, left) and $\Psi_N(\vec{r}) = -[i/(2V)^{1/2}](e^{i(3\pi/a)(x+y)} - e^{-i(3\pi/a)(x+y)}) = (2/V)^{1/2}\sin[3\pi/a(x+y)]$ (Figure 16a, right). The former has its electron density near most of the ions, the latter between most of the ions. Corresponding to each pair of peaks in the ⟨330⟩ set is a similar pair of states.

A mixing representative of the ⟨114⟩ diffraction peaks is shown in Figure 16b. The pair of free-electron states that mix to produce these pictures are $\psi_N(\vec{r}) = (1/V^{1/2})e^{i(\pi/a,\pi/a,4\pi/a)\cdot\vec{r}} = (1/V^{1/2})e^{i(\pi/a)(x+y+4z)}$ and $\psi_N(\vec{r}) = (1/V^{1/2})e^{i(-\pi/a,-\pi/a,-(4\pi/a))\cdot\vec{r}} = (1/V^{1/2})e^{-i(\pi/a)(x+y+4z)}$, which are again found at k-point N = $(\pi/a, \pi/a, 0)$. There is a subtle difference between the mixing shown in Figure 16b and the previous cases. Namely, the resulting cosine and sine waves are not aligned with the origin of the unit cell. That is, these mixed states resemble $\Psi_N(\vec{r}) = (2/V)^{1/2}\cos[(\pi/a)\text{-}(x+y+4z) + \alpha]$ and $\psi_N(\vec{r}) = (2/V)^{1/2}\sin[(\pi/a)(x+y+4z)+\alpha]$ with some phase factor α. This phase factor is needed to produce the same qualitative picture as before: one state whose electron density is near most of the ions (Figure 16b, left) and a second whose electron density is between most of the ions (Figure 16b, right).

Before proceeding to find these nearly free electron states within the LCAO band structure of Cu_5Zn_8, we should make one more point about these states. The reader might notice that all waves in Figure 16, whether they correspond to the ⟨330⟩ or ⟨114⟩ diffraction peaks, appear to have the same wavelength. This is indeed true, for the basic reason that $|\vec{k}|$ is inversely proportional to wavelength, and $|(3, 3, 0)| = |(1, 1, 4)|$. Because the energy of a plane-wave electronic state is proportional to $|\vec{k}|^2$, equal wavelengths translate to equal energies. It is vital to the MJ model that all waves that mix to produce Figure 16 have the same

dx.doi.org/10.1021/cr1001222 |Chem. Rev. XXXX, XXX, 000–000

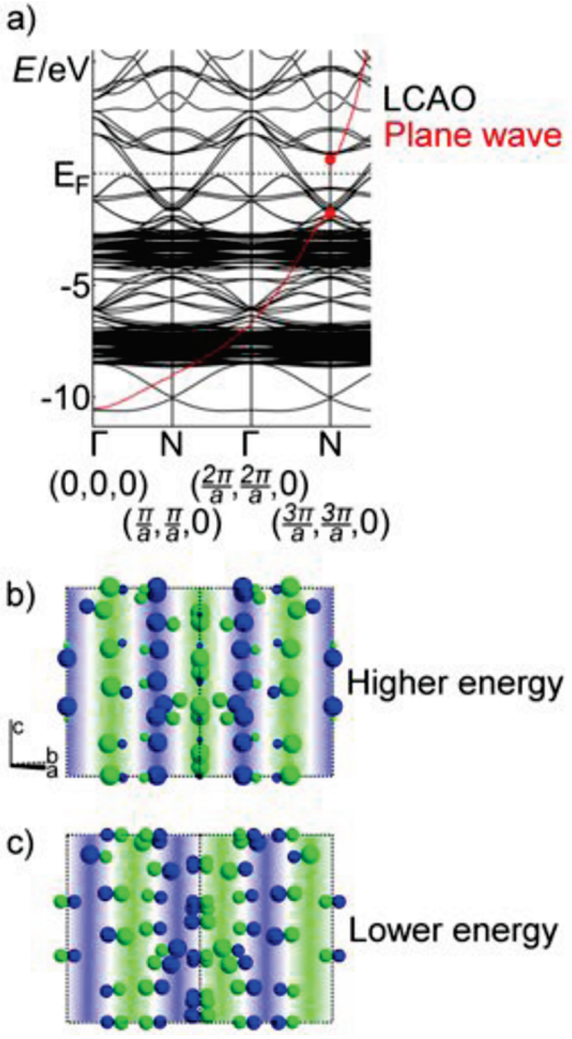

Figure 17. (a) The LCAO band structure of Cu_5Zn_8 (black) and the projected nearly free electron MJ band (red), plotted along a straight path through *k*-space from $\Gamma = (0, 0, 0)$ through $N = (3\pi/a, 3\pi/a, 0)$. (b, c) The two projected crystal orbitals at $N = (3\pi/a, 3\pi/a, 0)$, expressed as spheres that represent their component s and p atomic orbitals (see the text), with the corresponding nearly free electron waves shown lightly in the background. The energies of these two states straddle the Fermi energy.

energy. In this way, when mixing causes their energies to split, they contribute to a pseudogap at a single energy.

While the premise and implementation of the MJ model for the γ-brasses are beautiful, we may ask: Does the model alone confirm, to the satisfaction of a typical chemist, that the nearly free electron states in Figure 16 drive the stability of the Cu_5Zn_8 valence electron count? Probably not. To most chemists, it is important to see how this theoretical framework plays out within a quantum calculation of Cu_5Zn_8. For this, we employ the same procedure we used earlier for CuZn to extract the relevant MJ states and energies from the complex tangle that is the LCAO band structure of Cu_5Zn_8.

Figure 17 summarizes our LCAO interpretation of the MJ model as it relates to the ⟨330⟩ X-ray diffraction peaks in Cu_5Zn_8. In Figure 17a, the projected MJ band (red) is plotted on top of the LCAO band structure (black) along a straight path from $\vec{k} = (0, 0, 0)$ through $\vec{k} = (3\pi/a, 3\pi/a, 0)$. The MJ band resembles a nearly free electron parabola. Due to the mixing of

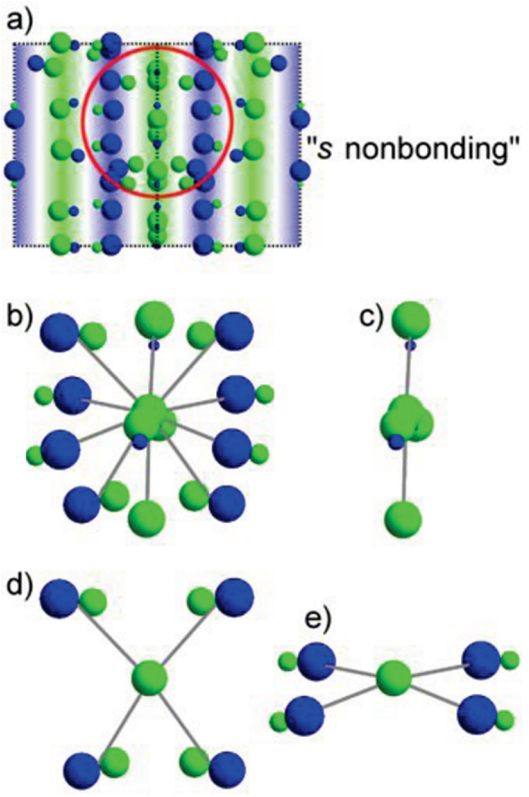

Figure 18. The local atomic orbital interactions of an IT Zn atom in Cu_5Zn_8 and its icosahedron of nearest neighbors in (a) the higher-energy projected MJ state at $N = (3\pi/a, 3\pi/a, 0)$, which is of primarily *s* character. (b) The 12 local interactions roughly break down as (c) σ-bonding, (d) nonbonding, and (e) σ-antibonding. Overall, the state is approximately nonbonding.

plane waves, the band has energy splittings at $N = (\pi/a, \pi/a, 0)$, $\Gamma = (2\pi/a, 2\pi/a, 0)$, and $N = (3\pi/a, 3\pi/a, 0)$ (the waves corresponding to the ⟨110⟩, ⟨220⟩, and ⟨330⟩ peaks). However, because the atoms in Cu_5Zn_8 do not interfere particularly constructively with the ⟨110⟩ or ⟨220⟩ diffraction plane waves, the energy splittings at $N = (\pi/a, \pi/a, 0)$ (0.15 eV) and $\Gamma = (2\pi/a, 2\pi/a, 0)$ (0.21 eV) are quite small. Due to the strong constructive interference of the atoms with the ⟨330⟩ diffraction plane waves, the splitting at $N = (3\pi/a, 3\pi/a, 0)$ (2.37 eV) is much larger. Also encouraging is that fact that the two projected states at this last *k*-point (red circles at −1.76 and 0.60 eV) straddle the Fermi energy and thus help stabilize Cu_5Zn_8 at 21/13 valence electrons per atom.

The two projected states at $N = (3\pi/a, 3\pi/a, 0)$ are displayed in Figure 17b,c. For ease of plotting, they are shown in a slightly different way than were the projected states in CuZn (Figure 8b,c). The component s and p orbitals on each atom that make up the projected states are shown not as contours of constant value of the wave function but as pairs of spheres whose volumes scale with the coefficients of the atomic orbitals. If the orbital on a given atom is purely s, it appears as a single sphere. If it is purely p, it appears as two spheres of equal size and opposite sign. If it is a mixture of s and p, is appears as two spheres of unequal size and opposite sign, skewed toward the sign of the s orbital. These two states resemble their nearly free electron wave analogs, shown lightly in the background. As was the case for CuZn, the higher-energy state (Figure 17b) is primarily a combination of s orbitals

dx.doi.org/10.1021/cr1001222 |*Chem. Rev.* XXXX, XXX, 000–000

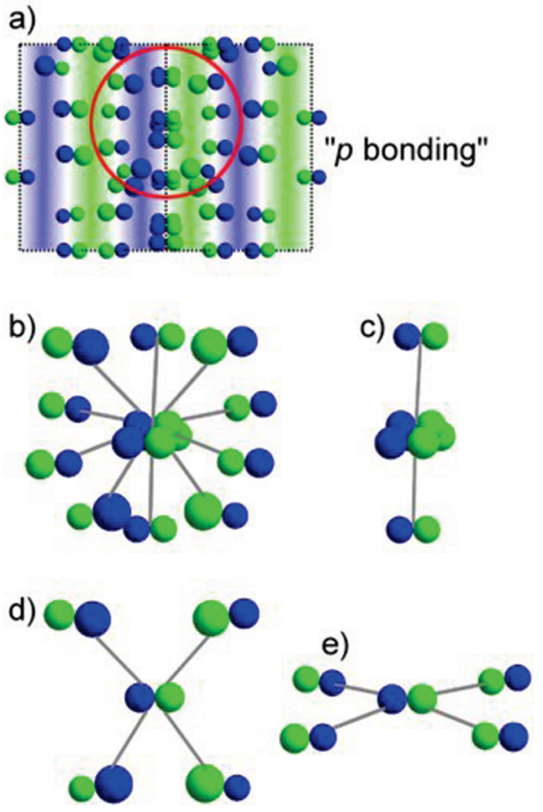

Figure 19. The local atomic orbital interactions of an IT Zn atom in Cu_5Zn_8 and its icosahedron of nearest neighbors in (a) the lower-energy projected MJ state at N = $(3\pi/a, 3\pi/a, 0)$, which is of primarily p character. (b) The 12 local interactions roughly break down as (c) π-bonding, (d) nonbonding, and (e) σ-bonding. Overall, the state is net bonding.

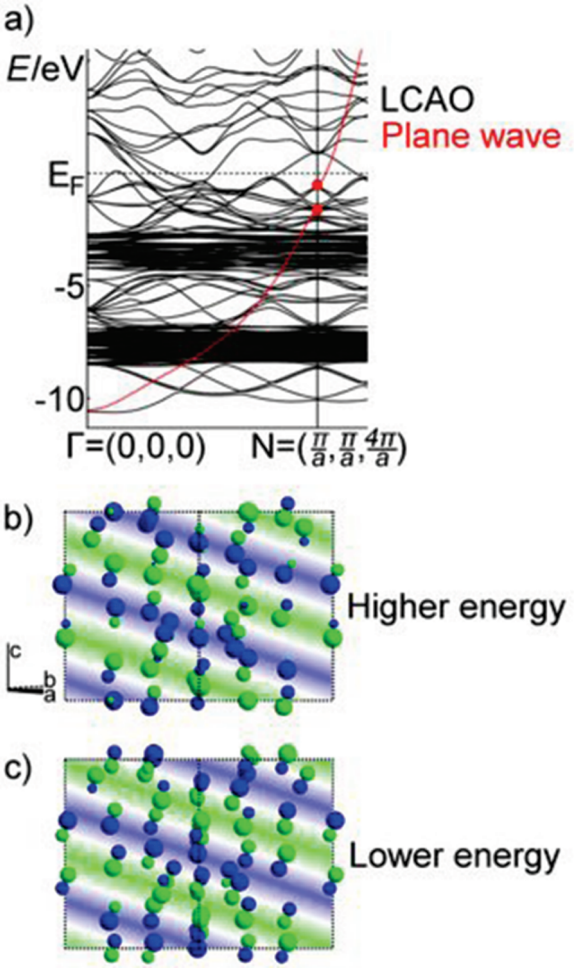

Figure 20. (a) The LCAO band structure of Cu_5Zn_8 (black) and the projected nearly free electron MJ band (red), plotted along a straight path through k-space from $\Gamma = (0, 0, 0)$ through N = $(\pi/a, \pi/a, 4\pi/a)$. (b, c) The two projected crystal orbitals at N = $(\pi/a, \pi/a, 4\pi/a)$, expressed as spheres that represent their component s and p atomic orbitals (see the text), with the corresponding nearly free electron waves shown lightly in the background. The energies of both states lie below the Fermi energy.

and the lower-energy state (Figure 17c) a combination of p orbitals. This ordering is again representative of the inverted region.

As in the CuZn case, it is worth noting the local atomic orbital interactions within these two wavelike projected states. Figure 18 deals with a particular region of the higher-energy state (Figure 18a)—an atom located at an IT site and its approximate icosahedron of 12 nearest neighbors (Figure 18b). Of these 12 interactions, four are primarily σ-bonding (Figure 18c), four nonbonding (Figure 18d), and four σ-antibonding (Figure 18e). Overall, this higher-energy state is roughly nonbonding. Figure 19 shows the analogous pictures of the same region of the lower-energy state (Figure 19a). Of the interactions between the same atom and its icosahedron of nearest neighbors (Figure 19b), four are primarily π-bonding (Figure 19c), four nonbonding (Figure 19d), and four σ-bonding (Figure 19e). In total, the lower-energy state is net bonding.

In Figure 20, we move on to the states corresponding to the ⟨114⟩ diffraction peaks in Cu_5Zn_8. The story here is more or less the same as it was for the ⟨330⟩ peaks. The projected MJ band (Figure 20a), when plotted along a straight path from $\vec{k}$ = (0, 0, 0) through $\vec{k}$ = $(\pi/a, \pi/a, 4\pi/a)$, resembles a nearly free electron parabola. The band splits by 1.03 eV at N = $(\pi/a, \pi/a, 4\pi/a)$, only about half the size of the splitting corresponding to the ⟨330⟩ peaks. This is to be expected, as the ⟨114⟩ peaks in Cu_5Zn_8 are less intense than ⟨330⟩. The two projected states at the top and bottom of this splitting are shown in Figure 20b,c. They again resemble their free-electron wave analogs, with the higher-energy state (Figure 20b) consisting primarily of s and the lower-energy state (Figure 20c) consisting primarily of p. This ordering is again in the inverted region.

In terms of local atomic orbital interactions, we can again see that the higher-energy of the two projected states is roughly nonbonding, while the lower energy of the two is bonding. Figure 21 shows interactions in the region of the higher-energy state (Figure 21a) between an IT atom and its icosahedron of nearest neighbors (Figure 21b). Four are primarily σ-bonding (Figure 21c), four nonbonding (Figure 21d), and four σ-antibonding (Figure 21e), for a total that is close to nonbonding. Figure 22 shows the analogous pictures of the same region of the lower-energy state (Figure 22a). Of the interactions between the same atom and its icosahedron of nearest neighbors (Figure 22b), four are primarily π-bonding (Figure 22c), four nonbonding (Figure 22d), and four σ-bonding (Figure 22e), for a total that is net bonding.

There is one significant way in which the projected states corresponding to the ⟨114⟩ X-ray diffraction peaks differ from

dx.doi.org/10.1021/cr1001222 |*Chem. Rev.* XXXX, XXX, 000–000

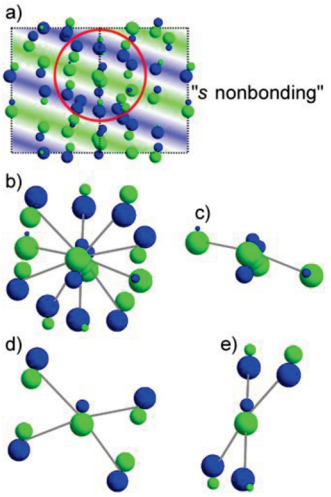

Figure 21. The local atomic orbital interactions of an IT Zn atom in Cu_5Zn_8 and its icosahedron of nearest neighbors in (a) the higher-energy projected MJ state at N = (π/a, π/a, $4\pi/a$), which is of primarily s character. (b) The 12 local interactions roughly break down as (c) σ-bonding, (d) nonbonding, and (e) σ-antibonding. Overall, the state is approximately nonbonding.

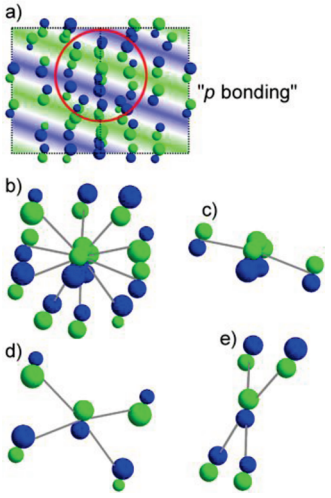

Figure 22. The local atomic orbital interactions of an IT Zn atom in Cu_5Zn_8 and its icosahedron of nearest neighbors in (a) the lower-energy projected MJ state at N = (π/a, π/a, $4\pi/a$), which is of primarily p character. (b) The 12 local interactions roughly break down as (c) π-bonding, (d) nonbonding, and (e) σ-bonding. Overall, the state is net bonding.

those corresponding to ⟨330⟩. Namely, the two projected states at N = (π/a, π/a, $4\pi/a$) (red circles in Figure 20a at −1.59 and −0.56 eV) both lie below the Fermi energy. This seems at first to be a strike against the MJ model or our interpretation of it, as it suggests that the energy splitting at this *k*-point does not stabilize Cu_5Zn_8 at its experimental electron count. But as the next subsection explains, this result need not be seen as problematic at all.

6.3. Energy Splitting at Other *k*-Points in Cu_5Zn_8

We showed earlier that MJ-type energy splitting occurs not just at isolated *k*-points but on the surface of the Jones zone. Because CuZn had only the strong ⟨110⟩ diffraction peaks

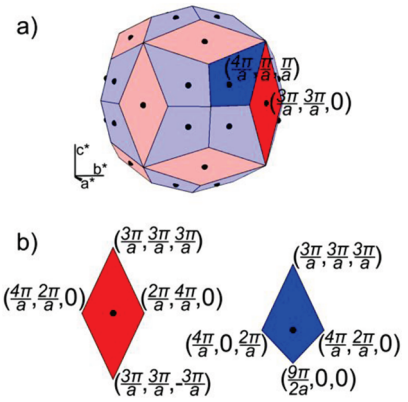

Figure 23. (a) The surface that separates the Cu_5Zn_8 nearly free electron states that are above the energy splitting (outside the Jones zone) from those that are below it (inside the Jones zone). (b) One of each type of face of the Jones zone, corresponding to the ⟨330⟩ (left, red) and ⟨114⟩ (right, blue) X-ray diffraction peaks.

corresponding to states near the Fermi energy, its Jones zone in Figure 10a had only one type of face. Cu_5Zn_8, however, has strong ⟨330⟩ and strong ⟨114⟩ peaks. Its Jones zone is therefore bounded by two symmetry-inequivalent types of faces.

The Cu_5Zn_8 Jones zone (Figure 23a) is shown with one of each type of face emphasized (Figure 23b). The 12 red faces correspond to the ⟨330⟩ reflections, while the 24 blue faces correspond to ⟨114⟩. One notable qualitative feature of this Cu_5Zn_8 Jones zone is that it is much closer to spherical than its CuZn counterpart. Due to its larger number of faces, the vertices of the Cu_5Zn_8 Jones zone do not jut out as much. The result is that the energy splitting on the surface occurs over a narrower range of energies for Cu_5Zn_8 than for CuZn. This can be seen in the respective densities of states, in which the pseudogap is sharper and more pronounced for Cu_5Zn_8 (Figure 14c) than for CuZn (Figure 5c).

In order to estimate the number of valence electrons this system is likely to hold, one might first assume that all states inside the Jones zone (below the energy splitting) are filled and all those outside the zone (above the energy splitting) are empty. If this is true, then the reciprocal-space volume of the Jones zone represents the number of filled valence orbitals per unit cell. The volume is $45(2\pi/a)^3$, or 45 unit cells of the reciprocal lattice. This translates to 90 valence electrons per unit cell, or 1.73 per atom—slightly higher than Hume-Rothery's empirical observations of the γ-brasses.

Once again, the assumption that all states at the bottom of the splitting are of lower energy than all states at the top of the splitting proves faulty. This is clear in Figure 24, in which we plot the top (gray) and bottom (black) of the energy splitting over the Jones zone faces corresponding to the ⟨330⟩ (Figure 24a) and ⟨114⟩ (Figure 24b) reflections. Even with a Jones zone that better approximates a sphere, there is still nowhere the Fermi energy can be placed such that it lies between the two paraboloids for all *k*-points simultaneously.

Because there is no true energy gap in the density of states of Cu_5Zn_8, the Fermi energy is likely to be found at a pseudogap. We expect such a pseudogap to be centered at an energy that lies within the splitting for most of the Jones zone surface. Inspection of the two different faces individually would lead one to arrive at two different estimates of the Fermi energy. For the surface corresponding to ⟨330⟩ (Figure 24a), it would be optimal to have

dx.doi.org/10.1021/cr1001222 |*Chem. Rev.* XXXX, XXX, 000–000

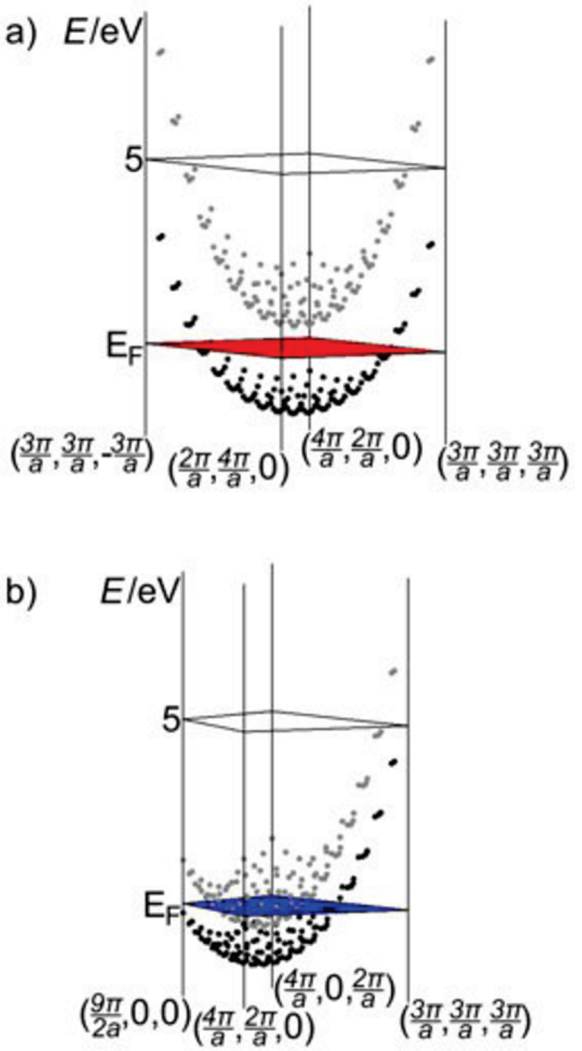

Figure 24. The energies at the top (gray) and bottom (black) of the splitting on the Jones zone faces of Cu_5Zn_8 corresponding to the (a) ⟨330⟩ and (b) ⟨114⟩ X-ray diffraction peaks. The Fermi energy (red and blue) lies between the paraboloids over much of the surfaces.

the Fermi energy just touch the bottom of the gray paraboloid, 0.60 eV above the actual Fermi energy. For the surface corresponding to ⟨114⟩ (Figure 24b), the bottom of the gray paraboloid is 0.56 eV below the actual Fermi energy. These estimates are confirmed in Figure 25a, which shows the area on each Jones zone face for which a given energy lies between the upper and lower curves. Taking both types of faces into account, we expect the actual Fermi energy to lie between 0.60 and −0.56 eV (1.68 and 1.49 valence electrons per atom, respectively)—a reassuring result.

It is difficult to pin down exactly where in this range the Fermi energy "should" lie for Cu_5Zn_8. One might make an estimate by finding the energy that maximizes the *total* Jones zone surface area that lies within the energy splitting. However, this estimate of the Fermi energy (Figure 25b) does not differ significantly from the estimate obtained by considering only the ⟨114⟩ faces and comes out on the low side of experimental reality. There are a number of ways in which this estimate is perhaps too simplistic, which are possible reasons for the discrepancy.

One possible oversimplification is in the way the energies on the Jones zone surface are calculated. As described earlier, the

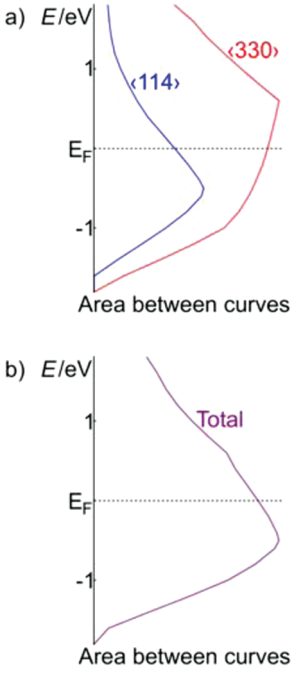

Figure 25. (a) The area on the Cu_5Zn_8 Jones zone faces corresponding to ⟨330⟩ and ⟨114⟩ for which a given energy lies within the splitting. (b) The area on the entire Jones zone surface for which a given energy lies within the splitting. Area is plotted in arbitrary units.

energies at the top and bottom of the gap reflect a mixing of two plane waves found on opposite faces of the Jones zone. While these pairs of waves are indeed the primary contributors to MJ-type energy splitting, the splitting could be made more accurate by including the contributions of other terms as well. This could mean including waves that correspond to weaker, but still significant, X-ray diffraction peaks. It could also mean including extra terms for points near the edges and vertices of the Jones zone, corresponding to the neighboring faces that approach each other. By considering only the pairwise mixing of plane waves, we likely underestimate the energy splitting, especially near edges and vertices of the Jones zone surface.

A second possible oversimplification is in our use of Jones zone surface area to estimate the pseudogap energy. This method, to look for the energy at which the largest amount of surface area lies within the splitting, neglects a key fact. When plane-wave states mix and split in energy, they do not simply disappear. Rather, they are pushed to an energy outside the splitting—likely *just* outside the splitting. So in considering whether a given energy would be an energetically stable Fermi energy, we must not only consider it favorable for the energy to lie within the splitting but also unfavorable for that energy to lie *just* outside the splitting.

One can imagine how our methods could be modified to account for each of these issues. To more accurately calculate the energies at the top and bottom of the gap, we could include more plane-wave terms in our mixing equations. To more correctly estimate the energy of the pseudogap, we could develop a slightly different method of counting surface area, in which area just outside the energy gap is disfavored. Even if we were to make these (and possibly other) adjustments, it is hard to say whether they would allow us to estimate valence electron counts and Fermi energies to greater numerical accuracy. Ultimately, these issues are not determined directly by the pseudogap energy but by the relative total energies of all possible structures.

dx.doi.org/10.1021/cr1001222 |*Chem. Rev.* XXXX, XXX, 000–000

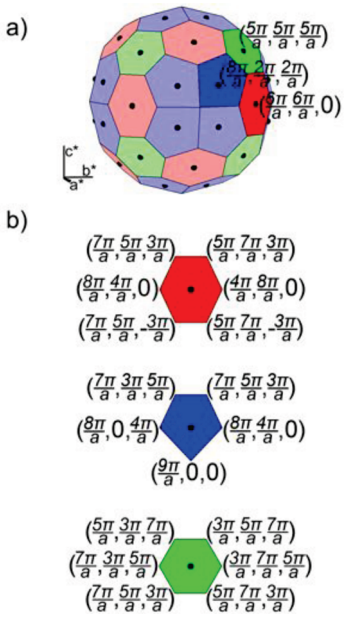

Figure 26. (a) The surface that separates the 2 × 2 × 2 γ-brass nearly free electron states that are above the energy splitting (outside the Jones zone) from those that are below it (inside the Jones zone). (b) One of each type of face of the Jones zone, corresponding to the ⟨660⟩ (top, red), ⟨228⟩ (middle, blue), and ⟨555⟩ (bottom, green) X-ray diffraction peaks.

7. ONWARD TO COMPLEXITY: THE 2 × 2 × 2 γ-BRASSES

We hope the previous sections of this account have convinced the reader that there is chemical importance to the electronic states on which the MJ model focuses. Even if the model and our LCAO interpretation of it cannot yet predict stable electron counts as precisely or as unambiguously as we would hope, they appear to be meaningful and qualitatively correct.

We therefore have certain expectations of how the same line of reasoning is likely to turn out for the 2 × 2 × 2 γ-brass superstructures. In the X-ray diffraction patterns of these compounds (Figure 13b), we saw that in addition to the strong ⟨660⟩ and ⟨228⟩ peaks derived from γ-brass itself, there are strong ⟨555⟩ peaks. These new peaks indicate more opportunities for MJ-type mixing, each of which contributes to the pseudogap that stabilizes the compounds at a given valence electron count. Figure 26 shows the Jones zone that marks the energy gap in the 2 × 2 × 2 γ-brasses (Figure 26a). It consists of three symmetry-inequivalent types of faces (Figure 26b): 12 faces corresponding to the ⟨660⟩ peaks (red), 24 faces corresponding to the ⟨228⟩ peaks (blue), and 8 faces corresponding to the ⟨555⟩ peaks (green).

With its relatively large number of faces, the Jones zone representing the 2 × 2 × 2 γ-brasses is quite nearly spherical. This should mean that the energy splitting occurs over a narrow range of energies and that the pseudogap in the density of states is quite sharp and pronounced. One would expect the number of valence orbitals per unit cell with energies lower than this pseudogap to be roughly equal to the Jones zone volume. The volume is $348(2\pi/a)^3$, meaning that the unit cell of 2 × 2 × 2 γ-brass holds 696 valence electrons. This is a reasonable estimate of the actual valence electron counts in many of the 2 × 2 × 2 γ-brasses: $Zn_{21}Pt_5$ (672 per unit cell, 1.62 per atom), $Li_{21}Si_5$ (656 per unit cell, 1.58 per atom), $Mg_{44}Rh_7$ (648 per unit cell, 1.59 per atom), $Mg_{44}Ir_7$ (648 per unit cell, 1.59 per atom), Mg_6Pd (679 per unit cell, 1.71 per atom), $Cu_{41}Sn_{11}$ (680 per unit cell, 1.63 per atom), $Mg_{29}Ir_4$ (648 per unit cell, 1.64 per atom), $Zn_{91}Ir_{11}$ (684 per unit cell, 1.68 per atom), and $Li_{13}Na_{29}Ba_{19}$ (640 per unit cell, 1.31 per atom). For technical reasons, it has proven difficult to extract precise information about the 2 × 2 × 2 γ-brasses from an LCAO calculation. For now, our suggestion that the electron counts of these compounds are driven by the same factors that guide CuZn and Cu_5Zn_8 therefore remains an inference.

8. CONCLUSION

In this work, we have reviewed Mott and Jones's theoretical model for Hume-Rothery electron phases, casting it into real-space LCAO language. In doing so, we have shown that the hallmark of an electron phase—a pseudogap in the density of states at the Fermi energy—can be seen not only in terms of the mixing and splitting of plane-wave electronic states, but also in terms of the energy difference between an s-based and a p-based band. This latter interpretation highlights the fundamental similarity between the Hume-Rothery rules in solids and the molecular electron-counting rules that are ingrained in the language and logic of chemists.

However, neither Mott and Jones's traditional model nor our LCAO interpretation of it does everything it sets out to do. That is to say, neither reproduces Hume-Rothery's electron-counting rules unambiguously or with much numerical precision. The likely reason for this is that both models focus on *pseudogap* energies of crystal structures, rather than their *total* energies. While related, it is only through a total energy comparison that one can determine which structure is favored over others at a given electron count.

We hope to achieve this goal—a rationale that accounts for the stability ranges of the Hume-Rothery electron phases—in our future work. Our LCAO interpretation of Mott and Jones's arguments will likely be an integral part of such a rationale, as it has already been shown that Hückel theory is capable of correctly ordering the total energies of these structures.[79,80]

We do not wish to suggest that either the nearly free electron or the LCAO viewpoint is superior. The two complement each other nicely, with the former focusing on the wavelike nature of the electronic states and the latter on the bonding and antibonding interactions between atomic orbitals. The two viewpoints arrive at similar conclusions, and in the end are distinguished only in subtle ways. Each has its advantages, and each allows one to understand certain aspects of the electronic structure of these compounds more clearly.

APPENDIX

In our analysis of γ-brass and its 2 × 2 × 2 superstructures, we have used information about their respective sets of strong X-ray diffraction peaks (Figure 13). For γ-brass, the dominant peaks are ⟨330⟩ and ⟨114⟩; for the 2 × 2 × 2 superstructures, they are ⟨660⟩, ⟨228⟩, and ⟨555⟩. But we have yet to explore *why* this is so. We would like to identify, from a qualitative real-space standpoint, the source of these strong peaks.

These sets of strong diffraction peaks are similar to each other in that the γ-brass ⟨330⟩ and ⟨114⟩ peaks become ⟨660⟩ and ⟨228⟩ when the unit cell is doubled in all three dimensions. However, they differ in that the ⟨555⟩ peaks in the 2 × 2 × 2 superstructures have no analog in γ-brass. In this Appendix, we therefore address two questions. First, what is the source of the strong ⟨330⟩ and ⟨114⟩ peaks in γ-brass? Second, what features of

dx.doi.org/10.1021/cr1001222 |*Chem. Rev.* XXXX, XXX, 000–000

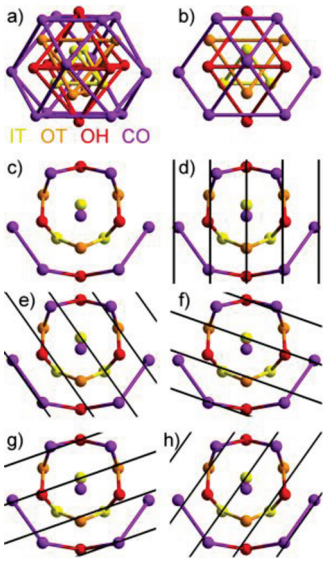

Figure 27. (a, b) Two views of a 26-atom γ-brass cluster, depicted as an inner tetrahedron (IT), an outer tetrahedron (OT), an octahedron (OH), and a cuboctahedron (CO). (c) An alternative connectivity of the cluster, highlighting its approximate 10-fold symmetry. (d−h) Five plane waves for which most of the cluster atoms lie near the crests.

the transformation from γ-brass to the $2 \times 2 \times 2$ γ-brasses bring about the intense $\langle 555 \rangle$ peaks?

The $\langle 330 \rangle$ and $\langle 114 \rangle$ Peaks in γ-Brass. With practice, the human eye is quite good at judging which X-ray diffraction peaks are strong for a given crystal structure. A strong peak is one for which most of the atomic positions lie near the crests of the plane wave corresponding to that peak. So in order to find the strong peaks in the ordered γ-brass phase Cu_5Zn_8, we must identify the directions in which the atoms lie on parallel planes. While this task is not so simple for a unit cell with many atoms, it can certainly be done.

Recall that the Cu_5Zn_8 structure has a cubic unit cell with a body-centered arrangement of two 26-atom γ-brass clusters. One γ-brass cluster is shown in Figure 27a, as four nested polyhedra. In anticipation of the discussion that follows, the cluster is shown from a slightly different viewpoint in Figure 27b. When γ-brass clusters are placed in unit cells, the viewpoint in Figure 27b is generally oriented along a face diagonal of the cell. From now on, we will consider this view (i.e., the direction normal to the page in Figure 27b) to be along the $[1\bar{1}0]$ direction. In Figure 27c, the cluster is connected in a way that illustrates an approximate 10-fold symmetry.[114] When shown with the viewpoint and connectivity of Figure 27c, the γ-brass cluster looks like a group of central atoms surrounded by a decagon and half of a second decagon.

The last five panels of this figure (Figure 27d−h) suggest five possible plane waves for which the cluster atoms lie mostly near the crests. In keeping with the approximate 10-fold symmetry of the cluster, the directions of these plane waves differ by 36°. These waves, along with all other symmetry-equivalent ones, could potentially correspond to strong diffraction peaks in a crystal structure with γ-brass clusters. However, this figure alone cannot identify the strong X-ray peaks for Cu_5Zn_8. Because diffraction is measured not for a single cluster but for an entire crystal, we must observe how these plane waves interact with all clusters in the unit cell.

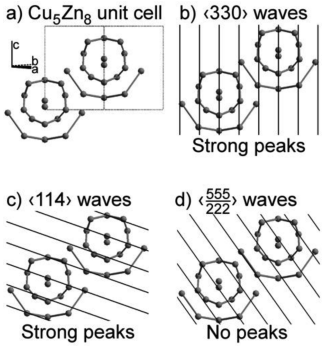

Figure 28. (a) The two γ-brass clusters in a cubic unit cell of Cu_5Zn_8. Representatives of the three unique sets of plane waves with constructive intracluster interference: (b) $\langle 330 \rangle$, (c) $\langle 114 \rangle$, and (d) $\langle 5/2\ 5/2\ 5/2 \rangle$. Of the three, $\langle 330 \rangle$ and $\langle 114 \rangle$ also have constructive intercluster interference and therefore strong X-ray diffraction peaks. However, $\langle 5/2\ 5/2\ 5/2 \rangle$ has destructive intercluster interference and therefore no diffraction intensity.

In keeping with its body-centered translational symmetry, the Cu_5Zn_8 structure has two γ-brass clusters centered at (0, 0, 0) and $(a/2, a/2, a/2)$ in the cubic unit cell (Figure 28a). For the five plane waves that sync up with the atoms of a single γ-brass cluster (Figure 27d−h), let us see how each wave interacts with the pair of clusters within a unit cell. In Figure 28b, the wave from Figure 27d is shown interacting with two clusters. The important result is that the wave's interactions with the two clusters are in phase with each other. That is, when the wave is positioned to have its crests aligned with the atoms in one cluster, its crests are consequently aligned with the atoms in the other cluster. Therefore, all γ-brass clusters in the Cu_5Zn_8 structure interfere constructively with this plane wave, resulting in a strong X-ray diffraction peak. As our view is in the $[1\bar{1}0]$ direction, this plane wave and this diffraction peak have Miller indices 330. By symmetry, the structure must have an entire set of 12 equally strong $\langle 330 \rangle$ peaks (all permutations of ± 3, ± 3, and 0).

By symmetry of the γ-brass clusters, the plane waves in Figure 27f,g are equivalent. We therefore show only one of them interacting with two clusters (Figure 28c). Once again, this wave's interactions with the two clusters are in phase, as the wave crests are aligned with the atoms in both clusters. Therefore, this plane wave, whose Miller indices are 114, corresponds to a strong X-ray diffraction peak. The entire set of 24 equivalent $\langle 114 \rangle$ peaks (all permutations of ± 1, ± 1, and ± 4) must be equally strong.

Lastly, we come to the two symmetry-equivalent plane waves in Figure 27e,h, one of which we show interacting with two clusters (Figure 28d). In contrast to the previous cases, this wave's interactions with the two clusters are not in phase. When the wave is positioned to have its crests aligned with the atoms in one cluster, its crests are not aligned with the atoms in the other. In other words, while the wave's intracluster interference is constructive, its intercluster interference is destructive. Consequently, this plane wave, whose Miller indices are 5/2 5/2 5/2, has no corresponding X-ray diffraction peak.[115]

Despite the relative complexity of the Cu_5Zn_8 structure, we have accounted for the dominant peaks in its X-ray diffraction pattern using real-space pictures. We now move on to the diffraction peaks of the significantly more complicated $2 \times 2 \times 2$ γ-brasses.

Cluster Inversion and the $\langle 555 \rangle$ Peaks in $2 \times 2 \times 2$ γ-Brasses. Of the $2 \times 2 \times 2$ γ-brass structures that have been solved by single crystal X-ray diffraction, $Zn_{21}Pt_5$[18,33] and $Li_{21}Si_5$[27,28] can be

dx.doi.org/10.1021/cr1001222 |Chem. Rev. XXXX, XXX, 000–000

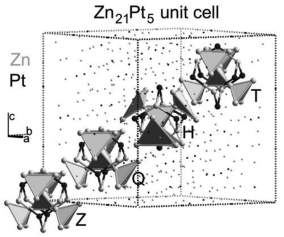

Figure 29. The cubic unit cell of $Zn_{21}Pt_5$, emphasizing four crystallographically inequivalent γ-brass clusters centered at Z = (0, 0, 0), Q = (a/4, a/4, a/4), H = (a/2, a/2, a/2), and T = (3a/4, 3a/4, 3a/4). The strongly distorted H cluster is shown in its more accurate inverted form. Pt atoms (black) occupy the ZOT, QOT, HOH, and TOH sites, while Zn atoms (gray) occupy the rest.

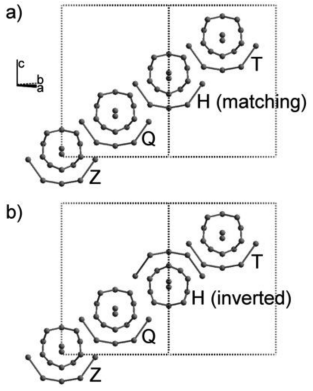

Figure 30. The four crystallographically inequivalent clusters in a cubic unit cell of 2 × 2 × 2 γ-brass, (a) with all four clusters oriented identically and (b) with the H cluster inverted with respect to the others.

compared most easily to Cu_5Zn_8, as they are built entirely of γ-brass clusters. We therefore focus our attention on $Zn_{21}Pt_5$ and $Li_{21}Si_5$, though any discussion of these structures for the remainder of this Appendix relates to other superstructures as well.

$Zn_{21}Pt_5$ and $Li_{21}Si_5$, very nearly identical to each other with the exception of the elemental identities, crystallize with $F\bar{4}3m$ symmetry. As the Cu_5Zn_8 unit cell contains two γ-brass clusters, those of the 2 × 2 × 2 γ-brasses contain 16 such clusters, a total of 416 atoms. By face-centered translational symmetry, these 16 clusters represent four crystallographically unique sets. One representative of each set in the unit cell of $Zn_{21}Pt_5$ is displayed in Figure 29. Using conventions we introduced in a previous paper,[68] we show the clusters centered at (0, 0, 0), (a/4, a/4, a/4), (a/2, a/2, a/2), and (3a/4, 3a/4, 3a/4), and refer to them as Z (*z*ero), Q (*q*uarter), H (*h*alf), and T (*t*hree quarters).

$Zn_{21}Pt_5$ and $Li_{21}Si_5$ share two key structural features that distinguish them from Cu_5Zn_8. The first one, and the focus of this section, is that the H cluster distorts to the point that it is more accurately shown as inverted with respect to the other clusters. In Figure 30, the clusters of 2 × 2 × 2 γ-brass are shown in two ways. Figure 30a is a simple doubling of the Cu_5Zn_8 unit cell in all three dimensions, with all clusters oriented exactly as they are in Cu_5Zn_8. The second panel (Figure 30b), which more accurately reflects the crystal structures of $Zn_{21}Pt_5$ and $Li_{21}Si_5$, shows the H cluster inverted with respect to the other three.

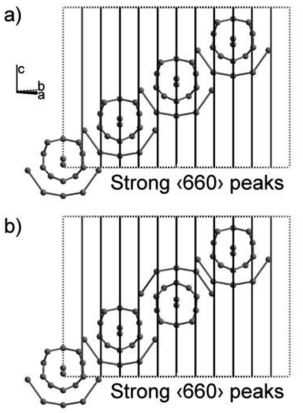

Figure 31. Interaction between the four clusters in 2 × 2 × 2 γ-brass and the ⟨660⟩ plane waves, (a) with all four clusters oriented identically and (b) with the H cluster inverted. In both cases, intra- and intercluster interference are constructive, leading to strong diffraction peaks.

This H cluster inversion seems at first surprising and mysterious. Why would it stabilize the structures electronically? For the answer, we turn to the X-ray diffraction patterns. As the Mott and Jones model dictates, the stability of electron phases is closely related to the strength of their diffraction peaks. Let us therefore examine the role inversion of the H cluster in creating strong ⟨660⟩, ⟨228⟩, and ⟨555⟩ peaks in the X-ray diffraction patterns of $Zn_{21}Pt_5$ and $Li_{21}Si_5$.

For Cu_5Zn_8, we have seen that the strongest peaks are ⟨330⟩ and ⟨114⟩. When the unit cell of Cu_5Zn_8 is doubled in all three dimensions without changing the atomic positions (Figure 30a), the diffraction intensities cannot change. Without inversion of the H cluster, we therefore expect 2 × 2 × 2 γ-brass to have the same strong peaks as γ-brass itself. The labels of these peaks change, however, taking on the Miller indices ⟨660⟩ and ⟨228⟩ in the new unit cell. By recognizing that ⟨660⟩ and ⟨228⟩ are simply the strong peaks of Cu_5Zn_8, we are well on our way to understanding the diffraction patterns of $Zn_{21}Pt_5$ and $Li_{21}Si_5$. What remains is to explain how inversion of the H cluster allows the ⟨660⟩ and ⟨228⟩ to remain strong while also creating strong ⟨555⟩ peaks. We illustrate this in a series of three figures.

The first of these figures (Figure 31) deals with the ⟨660⟩ peaks. Regardless of whether all four γ-brass clusters have the same orientation (Figure 31a) or the H cluster is inverted (Figure 31b), all clusters interfere constructively with the ⟨660⟩ plane waves, resulting in strong ⟨660⟩ peaks. The same is true of the ⟨228⟩ peaks (Figure 32). When all four γ-brass clusters have the same orientation (Figure 32a), they all interfere constructively with the ⟨228⟩ plane waves. When the H cluster is inverted (Figure 32b), its atoms still sync up almost as well with the wave crests, allowing the ⟨228⟩ peaks to remain strong.

Finally, we come to the ⟨555⟩ peaks (Figure 33), the major distinguishing feature of 2 × 2 × 2 γ-brass X-ray diffraction patterns as compared to γ-brass. When all four clusters are identical (Figure 33a), the ⟨555⟩ peaks have no intensity. This can be seen in the destructive intercluster interference with the ⟨555⟩ plane waves.[116] Take special note of the fact that the Z and H clusters cancel each other out by having most of the Z atoms near wave crests and most of the H atoms near wave troughs. Now, consider what happens when the H cluster is inverted (Figure 33b). The H cluster atoms now reside near wave crests,

dx.doi.org/10.1021/cr1001222 |*Chem. Rev.* XXXX, XXX, 000–000

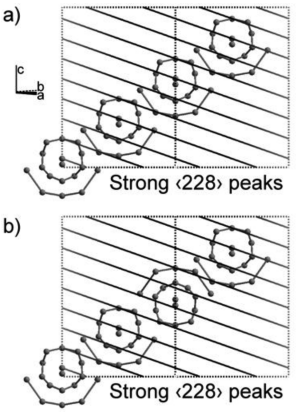

Figure 32. Interaction between the four clusters in 2 × 2 × 2 γ-brass and the ⟨228⟩ plane waves, (a) with all four clusters oriented identically and (b) with the H cluster inverted. In both cases, intra- and intercluster interference are constructive, leading to strong diffraction peaks.

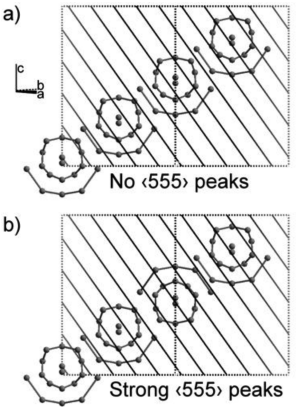

Figure 33. Interaction between the four clusters in 2 × 2 × 2 γ-brass and the ⟨555⟩ plane waves, (a) with all four clusters oriented identically and (b) with the H cluster inverted. While both pictures have good intracluster interference, only the second has the constructive intercluster interference required to create strong diffraction peaks.

making the previously nonexistent ⟨555⟩ peaks relatively intense. The emergence of strong ⟨555⟩ peaks in $Zn_{21}Pt_5$ and $Li_{21}Si_5$ can thus be rationalized using the inversion of the H cluster.

The Role of Coloring in the Diffraction Patterns of 2 × 2 × 2 γ-Brasses. So far, we have been concerned only with atomic positions, and not with which elements lie at which sites. We have implicitly assumed that all atoms scatter X-rays equally, which is of course not true. An atom's scattering factor is related to its number of electrons. So when a compound has two elements of very different numbers of electrons, as do $Zn_{21}Pt_5$ and $Li_{21}Si_5$, its X-ray diffraction pattern is strongly influenced by the site preferences of the constituent elements. Specifically, when one determines the strength of an X-ray peak by observing how well the atoms sync up with the peaks of a plane wave, one must consider the placement of heavier atoms to be more important.

This brings us to the second feature that distingishes $Zn_{21}Pt_5$ and $Li_{21}Si_5$ from Cu_5Zn_8. In both superstructures, the heavy element (i.e., Pt or Si) occupies four crytsallographic sites: the outer tetrahedron of the Z cluster (ZOT), the outer tetrahedron of the Q cluster (QOT),

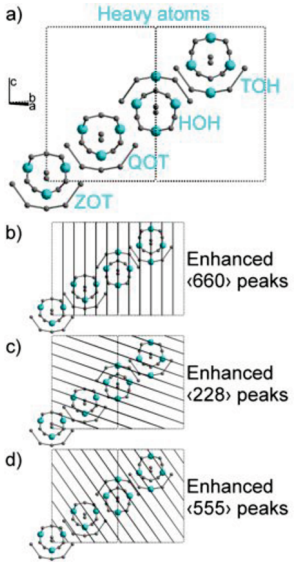

Figure 34. (a) The experimentally observed site positions of the heavier element in $Zn_{21}Pt_5$ and $Li_{21}Si_5$, shown in cyan. These four sites (ZOT, QOT, HOH, and TOH) align particularly well with the crests of the (b) ⟨660⟩, (c) ⟨228⟩, and (d) ⟨555⟩ plane waves, strengthening the intensities of the corresponding X-ray diffraction peaks.

the octahedron of the H cluster (HOH), and the octahedron of the T cluster (TOH) (Figure 34a). As we will now see, these heavy atoms are positioned in such a way that they strengthen the already strong ⟨660⟩, ⟨228⟩, and ⟨555⟩ diffraction peaks.

As Figure 34b shows, these four heavy atom sites are exceptionally in phase with the ⟨660⟩ plane waves, with every heavy atom lying almost exactly on a crest. Because heavy atoms have extra importance in determining the strength of diffraction peaks, we expect this pattern of site occupancy to strengthen the ⟨660⟩ peaks of $Zn_{21}Pt_5$ and $Li_{21}Si_5$. There is, however, a caveat to this conclusion. Because the ⟨660⟩ plane waves interact equivalently with all four clusters, the peaks would be similarly enhanced if the heavy atoms were found on any combination of OT and OH sites. All the ⟨660⟩ peaks can tell us is that they are enhanced when the heavy atoms are found on OT and OH sites.

A similar story can be told of the ⟨228⟩ peaks (Figure 34c). As nearly all the heavy atoms in $Zn_{21}Pt_5$ and $Li_{21}Si_5$ are found very close to the crests of the ⟨228⟩ plane waves, we expect the ⟨228⟩ peaks to be strengthened. But once again, we should not read too much into this conclusion. Except for the H cluster (which is inverted), the ⟨228⟩ plane waves interact equivalently with all clusters. This means the ⟨228⟩ peaks would be enhanced by the placement of heavy atoms on any combination of OT and OH sites. The lone exception is that, due to the inversion of the H cluster, the placement of heavy atoms on HOT would interfere destructively with these waves. Indeed, heavy atoms are not found on HOT in $Zn_{21}Pt_5$ or $Li_{21}Si_5$.

As was the case for inversion of the H cluster, the strongest argument for the ZOT−QOT−HOH−TOH heavy atom occupancy pattern is in the ⟨555⟩ diffraction peaks. As Figure 34d shows, the heavy atoms line up well with the crests of the ⟨555⟩ plane waves, enhancing the ⟨555⟩ peaks. What is important here is that the ⟨555⟩ waves are in a slightly different phase with respect to each of the four clusters. While the OT atoms of the Z and Q clusters line up with the ⟨555⟩ wave crests, the OH atoms do not. And while the OH atoms of the H and T clusters line up with the ⟨555⟩ wave crests, the OT atoms do not. Therefore, the experimentally observed

dx.doi.org/10.1021/cr1001222 |*Chem. Rev.* XXXX, XXX, 000–000

ZOT−QOT−HOH−TOH heavy atom occupancy pattern is the optimal one for enhancing the ⟨555⟩ peaks in $Zn_{21}Pt_5$ and $Li_{21}Si_5$.

Throughout this paper, we have seen how Mott and Jones's arguments and our LCAO interpretation of them can be used to rationalize complex crystal structures. The results in this Appendix suggest ways in which the models might be taken a step further, to solve or predict them. The features that stabilize filled states near the Fermi energy (atoms, especially electronegative ones, on parallel planes) are similar to those that strengthen X-ray diffraction peaks (atoms, especially heavy ones, on parallel planes). For a given stoichiometry and set of atomic positions, the experimental coloring pattern is therefore likely to be that which strengthens the relevant X-ray diffraction peaks.

AUTHOR INFORMATION

Corresponding Author

*E-mail: sl137@cornell.edu (S.L); rh34@cornell.edu (R.H.).

BIOGRAPHIES

Robert F. Berger was born in Massachusetts, and received his Bachelor's degree (2005) from Princeton University. He received his Ph.D. (2009) from Cornell University under the guidance of Profs. Stephen Lee and Roald Hoffmann, developing theoretical models to understand complex intermetallic crystal structures. He is now a postdoctoral researcher with Dr. Jeffrey Neaton at Lawrence Berkeley National Laboratory. His current work uses a variety of computational methods to explore the relationships between crystal and electronic structure in oxides of interest to solar energy conversion.

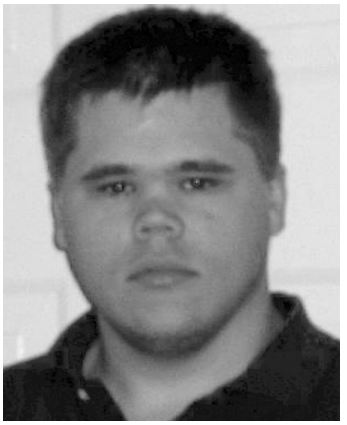

Peter L. Walters received his B.A. in chemistry from Cornell University in 2009. He is currently pursuing his Ph.D. degree in chemistry at the University of Illinois at Urbana−Champaign. His research interests include developing computational methods to explore the dynamics of complex quantum systems.

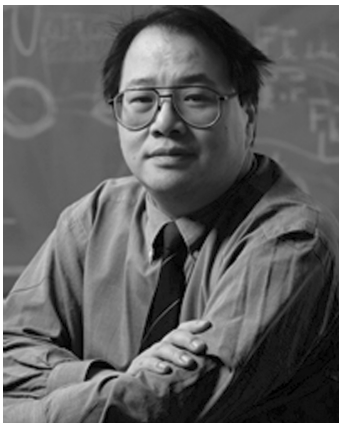

Stephen Lee is a Professor at Cornell University. He works on solid state chemistry.

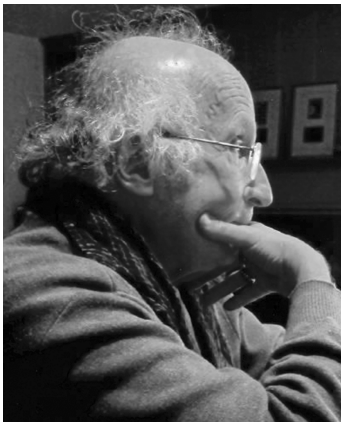

Roald Hoffmann is in his 46th year at Cornell University, now as the Frank H. T. Rhodes Professor of Humane Letters, Emeritus. He has not given up trying to build bridges between different parts of chemistry, chemistry and other sciences (and the sciences and the humanities), all the time respecting the individuality of the many ways of knowing that human beings have constructed, nor giving in to reductionism along the way. This paper, his first one in *Chemical Reviews*, is very much along these lines. Here we try to see, really see, the way the one true wave function of a system (a pretty complicated one at that, the γ-brasses) emerges from two seemingly disparate approximations—the chemical LCAO starting point or the physicists' perturbed free-electron model. We also hope to introduce chemists, gently, to the beauty of the Mott−Jones formalism.

ACKNOWLEDGMENT

This research was supported by the National Science Foundation through Grant DMR-0804223. We thank Prof. Neil Ashcroft for his careful reading of our work.

REFERENCES

(1) Hume-Rothery, W. *The Metallic State*; Clarendon Press: Oxford, UK, 1931.

(2) Hume-Rothery, W. *Electrons, Atoms, Metals and Alloys*; Dover: New York, 1963.

(3) Bradley, A.; Jones, P. *J. Inst. Met.* **1933**, *51*, 131.
(4) Hansen, M. *Constitution of Binary Alloys*; McGraw-Hill: New York, 1958.
(5) Samson, S. *Nature* **1962**, *195*, 259.
(6) Samson, S. *Acta Crystallogr.* **1965**, *19*, 401.
(7) Samson, S. *Acta Crystallogr.* **1967**, *23*, 586.
(8) Fredrickson, D. C.; Lee, S.; Hoffmann, R. *Angew. Chem., Int. Ed.* **2007**, *46*, 1958.
(9) Feuerbacher, M.; et al. *Z. Kristallogr.* **2007**, *222*, 259.
(10) Völlenkle, H.; Wittman, A.; Nowotny, H. *Monatsh. Chem.* **1967**, *98*, 176.
(11) Carl, W.; Schubert, K. *J. Less-Common Met.* **1969**, *19*, 279.
(12) Grin, Y. N.; Yarmolyuk, Y. P.; Zavodnik, V. E. *Kristallografiya* **1984**, *29*, 228.
(13) Fornasini, M. L.; Pani, M. *Acta Crystallogr.* **1986**, *C42*, 394.
(14) Cirafici, S.; Fornasini, M. L. *J. Less-Common Met.* **1989**, *154*, 79.
(15) Fornasini, M. L.; Mugnoli, A.; Palenzona, A. *J. Less-Common Met.* **1989**, *154*, 149.
(16) Gourdon, O.; Izaola, Z.; Elcoro, L.; Petricek, V.; Miller, G. J. *Philos. Mag.* **2006**, *86*, 419.
(17) Schmidt, J. T.; Lee, S.; Fredrickson, D. C.; Conrad, M.; Sun, J.; Harbrecht, B. *Chem.—Eur. J.* **2007**, *13*, 1394.
(18) Johansson, A.; Westman, S. *Acta Chem. Scand.* **1970**, *24*, 3471.
(19) Westin, L. *Chem. Scripta* **1971**, *1*, 127.
(20) Westin, L.; Erdshammar, L.-E. *Acta Chem. Scand.* **1972**, *26*, 3619.
(21) Samson, S.; Hansen, D. A. *Acta Crystallogr.* **1972**, *B28*, 930.
(22) Samson, S. *Acta Crystallogr.* **1972**, *B28*, 936.
(23) Arnberg, L.; Jonsson, A.; Westman, S. *Acta Chem. Scand. A* **1976**, *30*, 187.
(24) Booth, M. H.; Brandon, J. K.; Brizard, R. Y.; Chieh, C.; Pearson, W. B. *Acta Crystallogr.* **1977**, *B33*, 30.
(25) Fornasini, M. L.; Chabot, B.; Parthé, E. *Acta Crystallogr.* **1978**, *B34*, 2093.
(26) Koster, A. S.; Schoone, J. C. *Acta Crystallogr.* **1981**, *B37*, 1905.
(27) Ramirez, R.; Nesper, R.; von Schnering, H.-G. *Z. Naturforsch., A: Phys. Sci.* **1986**, *41a*, 1267.
(28) Nesper, R.; von Schnering, H.-G. *J. Solid State Chem.* **1987**, *70*, 48.
(29) Mahne, S.; Harbrecht, B. *J. Alloys Compd.* **1994**, *203*, 271.
(30) Lidin, S.; Jacob, M.; Larsson, A.-K. *Acta Crystallogr.* **1994**, *C50*, 340.
(31) Bonhomme, F.; Yvon, K. *J. Alloys Compd.* **1995**, *227*, L1.
(32) Nasch, T.; Jeitschko, W. *J. Solid State Chem.* **1999**, *143*, 95.
(33) Harbrecht, B.; Thimmaiah, S.; Armbrüster, M.; Pietzonka, C.; Lee, S. *Z. Anorg. Allg. Chem.* **2002**, *628*, 2744.
(34) Hornfeck, W.; Thimmaiah, S.; Lee, S.; Harbrecht, B. *Chem.—Eur. J.* **2004**, *10*, 4616.
(35) Smetana, V.; Babizhetskyy, V.; Vajenine, G. V.; Simon, A. *Angew. Chem., Int. Ed.* **2006**, *45*, 6051.
(36) Weber, T.; Dshemuchadse, J.; Kobas, M.; Conrad, M.; Harbrecht, B.; Steurer, W. *Acta Crystallogr.* **2009**, *B65*, 308.
(37) Conrad, M.; Harbrecht, B.; Weber, T.; Jung, D. Y.; Steurer, W. *Acta Crystallogr.* **2009**, *B65*, 318.
(38) Morton, A. J. *Phys. Status Solidi A* **1974**, *23*, 275.
(39) Morton, A. J. *Phys. Status Solidi A* **1975**, *31*, 661.
(40) Broddin, D.; van Tendeloo, G.; van Landuyt, J.; Amelinckx, S.; Portier, R.; Guymont, M.; Loiseau, A. *Philos. Mag. A* **1986**, *54*, 395.
(41) Jones, H. *Proc. R. Soc. A* **1934**, *144*, 225.
(42) Mott, N. F.; Jones, H. *The Theory of the Properties of Metals and Alloys*; Clarendon Press: Oxford, UK, 1936.
(43) Paxton, A. T.; Methfessel, M.; Pettifor, D. G. *Proc. R. Soc. A* **1997**, *453*, 1493.
(44) Takeuchi, T.; Sato, H.; Mizutani, U. *J. Alloys Compd.* **2002**, *342*, 355.
(45) Mizutani, U.; Takeuchi, T.; Sato, H. *Prog. Mater. Sci.* **2004**, *49*, 227.
(46) Mizutani, U.; Takeuchi, T.; Sato, H. *J. Non-Cryst. Solids* **2004**, *334−335*, 331.
(47) Asahi, R.; Sato, H.; Takeuchi, T.; Mizutani, U. *Phys. Rev. B* **2005**, *71*, 165103.
(48) Asahi, R.; Sato, H.; Takeuchi, T.; Mizutani, U. *Phys. Rev. B* **2005**, *72*, 125102.
(49) Mizutani, U.; Asahi, R.; Sato, H.; Takeuchi, T. *Phys. Rev. B* **2006**, *74*, 235119.
(50) Mizutani, U.; Asahi, R.; Sato, H.; Takeuchi, T. *Philos. Mag.* **2006**, *86*, 645.
(51) Blandin, A. In *Phase Stability in Metals and Alloys*; Rudman, P. S., Stringer, J., Jaffee, R. I., Eds.; McGraw-Hill: New York, 1967.
(52) Heine, V. In *Phase Stability in Metals and Alloys*; Rudman, P. S., Stringer, J., Jaffee, R. I., Eds.; McGraw-Hill: New York, 1967.
(53) Stroud, D.; Ashcroft, N. W. *J. Phys. F: Met. Phys.* **1971**, *1*, 113.
(54) Ashcroft, N. W. *Phys. Rev.* **1965**, *140*, A935.
(55) Hafner, J.; Jaswal, S. S.; Tegze, M.; Pflugi, A.; Krieg, J.; Oelhafen, P.; Güntherodt, H. J. *J. Phys. F: Met. Phys.* **1988**, *18*, 2583.
(56) Ashcroft, N. W. *Phys. Rev. B* **1989**, *39*, 10552.
(57) Werkman, R. D.; Schurer, P. J.; Vincze, I.; van der Woude, F. *Hyperfine Interact.* **1989**, *45*, 409.
(58) Ossi, P. M.; Kothari, D. C. *J. Less-Common Met.* **1991**, *171*, 221.
(59) Jiang, Q.; Chi, B. Q.; Li, J. C. *Appl. Phys. Lett.* **2003**, *82*, 2984.
(60) Laissardière, G. T.; Nguyen-Manh, D.; Mayou, D. *Prog. Mater. Sci.* **2005**, *50*, 679.
(61) Andersson, S. *Acta Crystallogr.* **1978**, *A34*, 833.
(62) Chabot, B.; Cenzual, K.; Parthé, E. *Acta Crystallogr.* **1981**, *A37*, 6.
(63) Shevchenko, V. Y.; Blatov, V. A.; Ilyushin, G. D. *Glass Phys. Chem.* **2009**, *35*, 1.
(64) Shevchenko, V. Y.; Blatov, V. A.; Ilyushin, G. D. *Struct. Chem.* **2009**, *20*, 975.
(65) Blatov, V. A.; Ilyushin, G. D.; Proserpio, D. M. *Inorg. Chem.* **2010**, *49*, 1811.
(66) Berger, R. F.; Lee, S.; Johnson, J.; Nebgen, B.; Sha, F.; Xu, J. *Chem.—Eur. J.* **2008**, *14*, 3908.
(67) Berger, R. F.; Lee, S.; Johnson, J.; Nebgen, B.; So, A. C.-Y. *Chem.—Eur. J.* **2008**, *14*, 6627.
(68) Berger, R. F.; Lee, S.; Hoffmann, R. *Chem.—Eur. J.* **2007**, *13*, 7852.
(69) Gourdon, O.; Gout, D.; Williams, D. J.; Proffen, T.; Hobbs, S.; Miller, G. J. *Inorg. Chem.* **2007**, *46*, 251.
(70) Lewis, G. N. *J. Am. Chem. Soc.* **1916**, *38*, 762.
(71) Langmuir, I. *J. Am. Chem. Soc.* **1919**, *41*, 868.
(72) Langmuir, I. *Science* **1921**, *54*, 59.
(73) Hückel, E. *Z. Phys.* **1931**, *70*, 204.
(74) Hückel, E. *Z. Phys.* **1931**, *72*, 310.
(75) Hückel, E. *Z. Phys.* **1932**, *76*, 628.
(76) Wade, K. *J. Chem. Soc. D: Chem. Commun.* **1971**, *15*, 792.
(77) Mingos, D. M. P. *Nat. Phys. Sci.* **1972**, *236*, 99.
(78) Albright, T. A.; Burdett, J. K.; Whangbo, M.-H. *Orbital Interactions in Chemistry*; John Wiley & Sons: New York, 1985.
(79) Hoistad, L.; Lee, S. *J. Am. Chem. Soc.* **1991**, *113*, 8216.
(80) Lee, S.; Hoistad, L. *J. Alloys Compd.* **1995**, *229*, 66.
(81) Burdett, J. K. *Chemical Bonding in Solids*; Oxford University Press: Oxford, UK, 1995.
(82) Sato, H.; Takeuchi, T.; Mizutani, U. *Phys. Rev. B* **2004**, *70*, 024210.
(83) Feng, J. Ph.D. thesis, Cornell University: Ithaca, NY, 2007.
(84) In practice, one should use boundary conditions consistent with the symmetry of the problem at hand, to avoid introducing new degeneracies.
(85) Ashcroft, N. W.; Mermin, N. *Solid State Physics*; Saunders College Publishing: New York, 1976.
(86) Kittel, C. *Introduction to Solid State Physics*; John Wiley & Sons: New York, NY, 2005.
(87) Models have been proposed that allow a reversal of this energy ordering. For example, one can construct pseudopotentials in which a repulsive core-orthogonality contribution in the ionic cores nearly cancels the attractive ionic contribution.[117]
(88) Hoffmann, R. *J. Chem. Phys.* **1963**, *39*, 1397.
(89) Hoffmann, R. *Solids and Surfaces: A Chemist's View of Bonding in Extended Structures*; VCH: New York, 1988.

(90) For ease of representation, we show the crystal orbitals only at $k_x = 0$ and $k_x = \pi/a$. At other values of k_x, the atomic orbitals have complex coefficients and are therefore more difficult to represent.
(91) Brennan, T. D.; Burdett, J. K. *Inorg. Chem.* **1993**, *32*, 746.
(92) In a periodic potential, the states that are allowed to mix are those whose k_x are separated by a reciprocal lattice vector (i.e., an integral multiple of $2\pi/a$). Therefore, the $k_x = 0.99\pi/a$ and $k_x = -1.01\pi/a$ states mix strongly, the $k_x = 1.01\pi/a$ and $k_x = 0.99\pi/a$ states mix strongly, etc.
(93) Ackland, G. J.; Macleod, I. R. *New J. Phys.* **2004**, *6*, 138.
(94) Degtyareva, V. F. *Phys.-Uspekhi* **2006**, *49*, 369.
(95) Feng, J.; Hennig, R. G.; Ashcroft, N. W.; Hoffmann, R. *Nature* **2008**, *451*, 445.
(96) Feng, J.; Hoffmann, R.; Ashcroft, N. W. *J. Chem. Phys.* **2010**, *132*, 114106.
(97) Beck, L. H.; Smith, C. S. *Trans. AIME* **1952**, *194*, 1079.
(98) Valence electron counts of one and two electrons per atom are also fairly common among intermetallic CsCl-type phases, such as ZnNi and AlAu, respectively.
(99) Villars, P.; Calvert, L. D. *Pearson's Handbook of Crystallographic Data for Intermetallic Phases*, 2nd ed.; ASM International: Materials Park, OH, 1991.
(100) Kresse, G.; Hafner, J. *Phys. Rev. B* **1993**, *47*, 558.
(101) Kresse, G.; Hafner, J. *Phys. Rev. B* **1994**, *49*, 14251.
(102) Kresse, G.; Furthmüller, J. *Comput. Mater. Sci.* **1995**, *6*, 15.
(103) Kresse, G.; Furthmüller, J. *Phys. Rev. B* **1996**, *54*, 11169.
(104) Vanderbilt, D. *Phys. Rev. B* **1990**, *41*, 7892.
(105) Given the near-absence of ⟨100⟩ diffraction peaks, one may wonder why CuZn would order in the CsCl structure. Indeed, MJ-type approaches alone could not have predicted this detail.
(106) Fredrickson, D. C.; Lee, S.; Hoffmann, R.; Lin, J. *Inorg. Chem.* **2004**, *43*, 6151.
(107) Fredrickson, D. C.; Lee, S.; Hoffmann, R. *Inorg. Chem.* **2004**, *43*, 6159.
(108) Clark, P. M.; Lee, S.; Fredrickson, D. C. *J. Solid State Chem.* **2005**, *178*, 1269.
(109) Strictly speaking, sums of plane waves cannot be *exactly* expressed as sums of valence orbitals because a finite basis of valence orbitals does not span the function space.
(110) Because the basis functions of an LCAO calculation are Slater-type atomic orbitals, they lack the radial nodes one would find in a true 4s or 4p state.
(111) Canadell, E.; Whangbo, M.-H. *Chem. Rev.* **1991**, *91*, 965.
(112) Lee, S. *Acc. Chem. Res.* **1991**, *24*, 249.
(113) von Heidenstam, O.; Johansson, A.; Westman, S. *Acta Chem. Scand.* **1968**, *22*, 653.
(114) While we do not dwell on it here, this pseudosymmetry is remarkable in its own right, and we have studied it in greater depth in the past.[66]
(115) Those familiar with diffraction theory will recognize that such a plane wave, with noninteger Miller indices, cannot have any diffraction intensity, regardless of whether or not the cell is body-centered. No matter which way one thinks about it, the underlying reason for this lack of a diffraction peak is the same—this plane wave cannot simultaneously sync up with all γ-brass clusters in the Cu_5Zn_8 structure.
(116) For a more convincing argument that ⟨555⟩ can have no diffraction intensity when all clusters are identical, recall that Cu_5Zn_8 cannot have ⟨5/2 5/2 5/2⟩ peaks.
(117) Pettifor, D. G. *Bonding and Structure of Molecules and Solids*; Clarendon Press: Oxford, UK, 1995.